

UC Berkeley

UC Berkeley Previously Published Works

Title

Remotely sensed phenological heterogeneity of restored wetlands: linking vegetation structure and function

Permalink

<https://escholarship.org/uc/item/4v5934fz>

Authors

Dronova, Iryna
Taddeo, Sophie
Hemes, Kyle S
[et al.](#)

Publication Date

2021

DOI

10.1016/j.agrformet.2020.108215

Peer reviewed

1 **Remotely sensed phenological heterogeneity of restored wetlands:**
2 **linking vegetation structure and function**

3

4 Iryna Dronova^{1,2*}, Sophie Taddeo^{2,3}, Kyle S. Hemes^{1,4}, Sara H. Knox⁵, Alex
5 Valach¹, Patricia Y. Oikawa⁶, Kuno Kasak^{1,7}, Dennis D. Baldocchi¹

6

7 ¹Division of Ecosystem Science, Department of Environmental Science, Policy
8 and Management, College of Natural Resources, University of California
9 Berkeley, Berkeley CA 94720-3114

10 ²Department of Landscape Architecture and Environmental Planning, College
11 of Environmental Design, University of California Berkeley, Berkeley CA
12 94720-2000

13 ³Plant Science and Conservation, Chicago Botanic Garden, Glencoe, IL 60022,
14 USA

15 ⁴Stanford Woods Institute for the Environment, Stanford University, Stanford,
16 CA 94305, USA

17 ⁵Department of Geography, The University of British Columbia, Vancouver
18 BC, Canada, V6T 1Z2

19 ⁶Department of Earth and Environmental Sciences, California State
20 University, East Bay,
21 Hayward, CA 94542

22 ⁷Department of Geography, University of Tartu, Vanemuise 46, 50410, Tartu,
23 Estonia

24

25

*corresponding author, email: idonova@berkeley.edu

26

27 **Abstract**

28 Seasonal phenological dynamics of vegetation hold important clues on
29 ecosystem performance towards management goals, like carbon uptake, and
30 thus should be considered in projections of their targeted services. However,
31 in wetlands spatio-temporal heterogeneity due to mixing of open water, soil,
32 green and dead vegetation makes it difficult to generalize ecosystem
33 functioning across different regions. Remote sensing observations can
34 provide spatially-explicit, cost-effective phenology indicators; however, little
35 is known about their capacity to indicate the links between wetland
36 ecosystem structure and function. Here we assessed this potential by
37 comparing one-year Enhanced Vegetation Index (EVI) from satellite products
38 at high (5m; RapidEye) and low (30m; Landsat) spatial resolutions with eddy
39 covariance time series of net carbon exchange, field digital camera
40 (phenocam) greenness and water temperature among three floristically
41 similar restored wetlands in California, USA. Phenological timing differed by
42 wetland site: depending on satellite, the range in site-median start of
43 greening was up to 28 days, end of greening - up to 73 days, start of
44 senescence - up to 79 days, and end of senescence - up to 10 days. Key
45 transition dates from satellite inputs agreed with seasonal changes in net
46 carbon exchange, phenocam greenness and water temperatures, suggesting
47 that phenological contrasts could result in part from site differences in
48 vegetation configuration and litter affecting the exposure of canopy, soil and
49 water to sunlight and thus sub-canopy microclimate and ecosystem

50 functioning. Yet, the agreement between satellite inputs was non-systematic,
51 with the greatest disparities at the more heterogeneous, less vegetated site.
52 Phenological model fitting uncertainty increased with greater spatial
53 resolution, highlighting the tradeoff between the accuracy of representing
54 vegetation and the complexity of local seasonal variation. These findings
55 highlight the sensitivity of satellite-derived phenology to structural and
56 functional heterogeneity of ecosystems and call for more rigorous spatially-
57 explicit analyses to inform assessments of restoration and management
58 outcomes.

59

60

61

62 **Keywords:** phenology; wetland; eddy covariance; heterogeneity; flux
63 footprint; remote sensing

64

65

66

67 **1. Introduction**

68 Remote sensing datasets, as they improve in temporal frequency, spatial
69 coverage and resolution, are increasingly used to model and upscale
70 ecosystem functions such as primary productivity and greenhouse gas fluxes
71 (Csillik et al., 2019; Knox et al., 2017; Wolf et al., 2016). Vegetation
72 phenology, or variation in plant cycles following seasonal and inter-annual
73 environmental dynamics, can modulate these functions in space and time
74 (Keenan et al., 2014, 2012; Ma et al., 2017; Ryu et al., 2010), which can be
75 manifested in the changes in spectral indicators of plant greenness (Gu et
76 al., 2003; Melaas et al., 2018; Richardson et al., 2018; Vogelmann et al.,
77 2016). Remotely sensed phenological indicators have provided important
78 insights on ecosystem sensitivity to climatic fluctuations (Friedl et al., 2014;
79 Hufkens et al., 2012), disturbance (Kennedy et al., 2010; Sulla-Menashe et
80 al., 2014) and land cover/use shifts (Zhang et al., 2015; Zhang and Weng,
81 2016; Zhu, 2017), among other factors. However, phenological patterns may
82 be also sensitive to less well understood local effects of vegetation structure
83 on solar energy transfer and microclimate, which may produce heterogeneity
84 in ecosystem functioning, particularly in areas with complex environmental
85 and floristic gradients (Huesca et al., 2015; Richardson et al., 2012; Tóth,
86 2018; Vrieling et al., 2018). To accurately model biogeochemical processes
87 and ecosystem services across scales, it is critical to better understand the
88 relationships between remotely sensed phenological complexity and on-the-

89 ground ecosystem properties contributing to their dynamics and
90 management responses.

91 Restored wetlands present a particularly interesting and important case
92 study to examine the phenological complexity and its implications for
93 ecosystem functions targeted by management. Restoration has been
94 globally expanding as a strategy to mitigate wetland losses and re-create
95 their critical services such as carbon sequestration, ecological habitats,
96 hydrological functions and coastal flood protection (Deverel et al., 2017;
97 Hemes et al., 2019; Klemas, 2013; Miller and Fujii, 2010; Villa and Bernal,
98 2018). However, as any ecological perturbation, restoration may lead to
99 substantial spatio-temporal variability in ecosystem structure and function,
100 particularly early in the recovery (Chamberlain et al., 2018; Chapple and
101 Dronova, 2017; Dronova and Taddeo, 2016; Eichelmann et al., 2018; Suding,
102 2011; Zhao et al., 2016). Restored systems with varying degree of spatial
103 heterogeneity thus offer a prime setting to study the impact of phenological
104 complexity on ecosystem functions. Leveraging remote sensing to assess
105 restoration outcomes in a spatially-explicit manner is critical to expand the
106 scope of monitoring efforts in heterogeneous, isolated, large, or sensitive
107 sites and to assess the progress towards targets or detect early signals of
108 undesirable shifts (Eichelmann et al., 2018; Hemes et al., 2019; Matthes et
109 al., 2014; McNicol et al., 2017; Taddeo and Dronova, 2019, 2018).

110 The relationship between vegetation structure and ecosystem function
111 during post-restoration recovery has been documented by several recent

112 studies in deciduous herbaceous marshes showing that change in the
113 relative coverage by plants versus open water affects surface energy
114 balance, evapotranspiration and water temperatures (Detto et al., 2006;
115 Eichelmann et al., 2018; Goulden et al., 2007; Hill and Payton, 2000;
116 Rejšková et al., 2012; Smesrud et al., 2014). In the absence of periodic
117 flushing, marshes dominated by reeds may also accumulate large amounts
118 of dead matter (litter) which affects canopy transfer of solar radiation and
119 thereby plant density, leaf area, aboveground productivity (Dronova and
120 Taddeo, 2016; Rocha et al., 2008; Rocha and Goulden, 2009; Schile et al.,
121 2013) and evapotranspiration (Eichelmann et al., 2018; Goulden et al.,
122 2007). Dense litter may substantially reduce sub-canopy soil and water
123 temperatures (Eichelmann et al., 2018; Goulden et al., 2007), affecting
124 seasonality of plant and microbial metabolism and thus the phenological
125 timing of plant establishment and growth (Flanagan et al., 2015; O'Connell et
126 al., 2019). Varying presence of litter and open water to vegetation coverage
127 can be expected to produce heterogeneity in the timing of phenological
128 transitions and ecosystem productivity even among floristically and
129 hydrologically similar wetlands.

130 Spatially explicit indicators of vegetation phenology derived from remote
131 sensing data could thus represent such structure-function feedbacks
132 (Butterfield and Malmstroem, 2009), as suggested by the previously reported
133 correlations between greenness and ecosystem function (Knox et al., 2017;
134 Ryu et al., 2010; Toomey et al., 2015) and the sensitivity of such correlations

135 to canopy structure and its effects on photosynthetic efficiency of plants
136 (Dronova et al., 2011; Dronova and Taddeo, 2016; LaRue et al., 2018; Rocha
137 et al., 2008; Smith et al., 2002). Phenologically informed indicators of
138 ecosystem function are also desirable for up-scaling local management
139 outcomes to broader regions of decision making (Byrd et al., 2014; Knox et
140 al., 2017; Richardson et al., 2012), at which assessment of 3-dimensional (3-
141 D) vegetation structure (e.g., with light detection and ranging (lidar)
142 systems) remains extremely costly. Fulfilling this potential requires a better
143 understanding of how the choice of a remote sensing product may affect
144 phenological interpretation depending on its spatial resolution and temporal
145 frequency, as well as landscape configuration of the target ecosystems
146 themselves. Historically popular imagery with 30+m spatial resolution has
147 limited sensitivity to spatial structure of complex systems such as wetlands;
148 yet the multi-decadal archives of such datasets provide nonparallel records
149 of the long-term site dynamics (Bolton et al., 2020; Melaas et al., 2016,
150 2013; Woodcock et al., 2020). In turn, emerging products offering both high
151 spatial resolution ($\leq 10\text{m}$) and high temporal frequency ($< 7\text{days}$) can make
152 spatially explicit phenological assessments more informative (Vrieling et al.
153 2018); however, it is not yet well understood to what extent the increase in
154 spatial detail might complicate phenological estimation or differ in outcomes
155 relative to the coarser-resolution inputs. Filling this gap becomes critical for
156 developing new image products from sensors that differ in spatial resolution

157 and temporal frequency but might be used interchangeably to assess
158 ecosystem performance (Bolton et al., 2020; Claverie et al., 2018).

159 In response to these needs, our study comparatively assessed
160 phenological characteristics in a set of restored freshwater wetlands in
161 California's Sacramento-San Joaquin Delta, USA (Figure 1) using one-year
162 imagery from two satellite products at high (5m) and moderate (30m) spatial
163 resolutions. To better understand the local sensitivity of phenology to the
164 feedbacks between structure and function, we also leveraged the time series
165 of net carbon exchange, water temperature, and digital photograph
166 (phenocam) greenness from the AmeriFlux eddy covariance stations. Our
167 objectives were to assess 1) whether satellite-based phenological indicators
168 of the greening and senescence timing differed among wetland sites with
169 varying configuration of vegetation patches; 2) to what extent phenological
170 metrics were sensitive to seasonal variation in ecosystem productivity
171 represented by the nearly continuous field-measured indicator of carbon
172 dioxide (CO₂) sequestration and phenocam spectral greenness, and 3) to
173 what extent remote sensing-based estimates of phenological timing agreed
174 between two satellite products with different spatial resolution. We expected
175 that wetlands with larger and more contiguous patches would reach seasonal
176 peaks of greenness and net CO₂ uptake later than wetlands with lower and
177 more fragmented vegetation coverage, due to greater likelihood of
178 accumulating litter which may restrict solar energy transfer and sub-canopy
179 water temperatures. Using our results, we further discuss the potential of

180 cost-effective satellite-derived phenological metrics to elucidate canopy
181 structure-function relationships in assessments of restoration outcomes in
182 heterogeneous ecosystems with limited site access and key future research
183 needs.

184 FIGURE 1 ABOUT HERE

185 **2. Methods**

186 **2.1. Study area and wetland sites**

187 This study was conducted in the Sacramento-San Joaquin Delta,
188 California, USA (hereafter the Delta), a region with Mediterranean climate
189 characterized by wet, cool winters and dry, hot summers which allow for
190 extensive cloud-free periods during the main growing season (March-
191 October). This region is currently undergoing extensive wetland restoration
192 efforts aimed at reversing land subsidence and re-establishing wildlife
193 habitat, recreational opportunities and other benefits (Bekaert et al., 2019;
194 Deverel, 2015; Deverel et al., 2010; Knox et al., 2015; Schaffer-Smith et al.,
195 2018; Sharma et al., 2016). Of particular interest is the potential of restored
196 wetlands to promote carbon sequestration and reduce emissions of
197 greenhouse gases (Hemes et al., 2019; Knox et al., 2017; Matthes et al.,
198 2014; Miller and Fujii, 2010; Oikawa et al., 2017), a goal shared across a
199 broader domain of emergent freshwater marshes (Chu et al., 2014; Franz et
200 al., 2016; Minke et al., 2016; Stefanik and Mitsch, 2012; Strachan et al.,
201 2015). Quantifying and projecting wetland ecosystem functioning at the
202 regional scale requires a deeper understanding of the role of spatio-temporal

203 complexity in wetland performance towards their management targets (Chu
204 et al., 2015; Matthes et al., 2014; McNicol et al., 2017).

205 Our study focused on three wetland sites (Table 1) in the western part of
206 the Delta (Figure 1) that had been established in 1997 (West Pond, or WP,
207 AmeriFlux code US-Tw1), 2010 (Mayberry Farms, or MB, code US-Myb) and
208 2014 (East End, or EE, code US-Tw4). Currently all of them function as
209 managed freshwater marshes excluded from tidal impacts, dominated by
210 cattails (*Typha* spp.) and tule (*Schoenoplectus acutus*) reeds. The sites differ
211 in size and initial design (Table 1); the oldest one was initially engineered as
212 a fully graded unit, half-planted with tule (Miller and Fujii, 2010), while the
213 other two sites were created with greater bathymetric complexity but no
214 specific design for emergent wetland vegetation (Dronova and Taddeo,
215 2016; Hemes et al., 2018; Knox et al., 2017). All these sites provide publicly
216 available AmeriFlux (<https://ameriflux.lbl.gov>) eddy covariance
217 measurements of the greenhouse gas carbon dioxide (CO₂), methane (CH₄)
218 and water vapor (H₂O) fluxes, as well as fixed-view above-canopy digital
219 photographs (phenocam data) and several ecosystem parameters, including
220 water temperature, administered by the UC Berkeley Biometeorology Lab.
221 Eddy covariance technique involves high temporal frequency measurements
222 of atmospheric concentrations of the abovementioned gases (using field-
223 mounted open-path gas analyzers) together with the three-dimensional wind
224 speed and several other environmental drivers (Baldocchi et al., 1988;
225 Hemes et al., 2019). These measurements can be converted to greenhouse

226 gas and carbon budgets for a given time frame of interest (e.g., daily) and
227 compared with phenological indicators derived from remote sensing images
228 (Gonsamo et al., 2013; Knox et al., 2017). Within each wetland site,
229 phenocam and water temperature data were collected at one location
230 associated with the eddy covariance flux station.

231 These wetlands provide a useful setting for comparing phenological
232 patterns because, despite their geographic proximity and similarities in
233 vegetation and hydrology, they markedly differ in their landscape surface
234 configuration (Eichelmann et al., 2018) due to varying size and geometry of
235 plant patches and vegetation structure (Table 1). The oldest wetland (19
236 years in 2016, WP) is nearly fully vegetated, and near the peak season of
237 2016 had the tallest canopy among the three sites (Table 1). In contrast, the
238 MB wetland (6-year old in 2016) is a mosaic of open water and smaller, more
239 geometrically complex vegetated patches (Figure 1) covering ~64% of the
240 whole site (Table 1). Plant canopies at MB had litter layers on average of
241 similar height as in WP, but shorter live vegetation and lower green leaf area
242 (Table 1). Finally, the youngest site (EE, 2 years in 2016) had the highest
243 green leaf area and shortest litter layer among the three wetlands (Table 1).
244 However, percent vegetation cover and mean patch size of EE were greater
245 than those of MB (Table 1), likely because this wetland experienced a rapid
246 colonization by *Typha* spp. in its first post-restoration summer and developed
247 relatively large patches that had persisted since.

248 TABLE 1 ABOUT HERE

249 2.2. Remote sensing data

250 We used two satellite remote sensing datasets for the year 2016 with high
251 frequency of cloud-free dates (Table A1, Appendix): 1) Landsat-8 Operational
252 Land Imager (OLI) Tier I surface reflectance product at 30m spatial
253 resolution, publicly available via the U.S. Geological Survey archive and
254 Google Earth Engine (Gorelick et al., 2017) catalog (16 dates), and 2)
255 RapidEye imagery at 5m spatial resolution provided by the Planet Labs
256 Education and Research Program (21 dates). The latter program by Planet
257 Labs Inc. allows researchers and educators to apply for non-commercial,
258 limited cost-free access to the RapidEye archive and Planetscope imagery for
259 various landscape analysis applications. In this study RapidEye data provided
260 a unique opportunity to assess wetland phenology at high spatial resolution
261 and temporal frequency and compare this inference with traditionally
262 popular 30-m Landsat data (e.g., Melaas et al., 2016, 2013; Mo et al., 2015).
263 Another reason for comparing these products was the length of their
264 missions' archives, covering substantial portions of the post-restoration
265 history of these sites (with Landsat 30-m data going back to mid-1980s and
266 RapidEye imagery - to 2009), which could facilitate longer-term multi-year
267 phenological analyses in the future.

268 All Landsat images in this study were from the same tile which
269 corresponded to path/row 44/34 in this satellite's World Reference System 2
270 and covered all three study sites. In turn, RapidEye data were selected so
271 that all three wetland sites were captured by the same dates. We then

272 converted each image individually from the at-sensor radiance to ground
273 surface reflectance using imagery metadata and 6S algorithm (Kotchenova
274 and Vermote, 2007), as surface reflectance product was not available from
275 the provider for 2016. Satellite images were clipped to the spatial extents of
276 the biometeorological flux footprints of each AmeriFlux eddy covariance
277 tower averaged for the year 2016, which resulted in 30, 81 and 30 Landsat
278 pixels and 928, 2234 and 784 RapidEye pixels for West Pond, Mayberry
279 Farms and East End, respectively (Supplementary Table S1). Flux footprints
280 represent areas of the landscape from which 90% of the flux originates, and
281 were generated using an analytical two-dimensional footprint model (Detto
282 et al., 2006; Hsieh et al., 2000; Knox et al., 2017). Each satellite image was
283 then converted into Enhanced Vegetation Index (EVI (1); Huete et al. 2002)
284 as a proxy of greenness:

$$285 \quad EVI = \frac{2.5 * (NIR - i)}{(NIR + 6 * i - 7.5 * i + 1)}, (1)$$

286 where *Blue*, *Red* and *NIR* indicate spectral reflectance in the blue (0.450-
287 0.515 μm for Landsat and 0.440-0.510 μm for RapidEye), red (0.630-0.680
288 μm for Landsat and 0.630-0.685 μm for RapidEye) and near-infrared (0.845-
289 0.885 μm for Landsat and 0.760-0.850 μm for RapidEye) electromagnetic
290 regions, respectively. EVI was selected due to its wide use in phenological
291 remote sensing studies (Klosterman et al., 2014; Melaas et al., 2018, 2016,
292 2013; Toomey et al., 2015), as it can circumvent important limitations of
293 other popular indices, particularly the tendency to saturate in closed

294 canopies (Huete et al., 2002). Furthermore, in an earlier study focusing on
295 two of our wetland sites, Landsat-based EVI showed stronger correlations
296 with gross primary productivity than a set of other satellite-derived indices
297 (Knox et al., 2017). Spectral indices and subsequent phenological metrics
298 (Table 2) were estimated in Matlab software version R2018b (MathWorks
299 Inc.).

300 FIGURE 2 ABOUT HERE

301 To identify pixels most likely to represent vegetation phenology, we
302 applied a spatial form of principal components analysis transformation
303 (Machado-Machado et al., 2011) to each image time series using all the
304 pixels within the flux footprints at the three sites. This transformation
305 produces a series of outcomes, or principal components (PCs) representing
306 common types of seasonal EVI trajectories in order of decreasing prevalence
307 (as indicated by variance explained by each PC), with the maximum possible
308 number of components equal to the number of pixels in a single-date image
309 within the flux footprint. As the dominant plant species of our wetland sites
310 were deciduous perennials, we focused on the “deciduous” trajectory with an
311 early-season increase in greenness during the greening phase and
312 subsequent decline in greenness during the senescence phase. For both
313 Landsat and RapidEye inputs, such a trajectory was captured by the first two
314 PCs which together accounted for 90.3% and 82% variation in each dataset,
315 respectively (Supplementary Figure S1). In contrast, the trajectories
316 captured by PCs 3 and 4 (Supplementary Figure S1) showed strongest

317 correlations with pixels from non-vegetated portions of roads and berms
 318 within the footprints. Pixels whose trajectories showed a linear correlation of
 319 0.7 or greater with either of the first two PCs were selected for subsequent
 320 phenological metric estimation. Among these, pixels with trajectories similar
 321 to PC1 were the overwhelming majority, occupying 70-100% of the flux
 322 footprints (Supplementary Table S1).

323 **2.3. Phenological metric estimation and comparison among** 324 **wetland sites**

325 Next, we estimated a set of phenological parameters for individual pixel
 326 seasonal trajectories by fitting the non-symmetrical double-logistic curves
 327 (Bauer et al., 2017; Head et al., 2004) to each satellite's EVI time series and
 328 interpolating EVI to a daily step:

$$329 \quad EVI(t) = P_1 + \frac{P_2}{1 + e^{P_3(P_{i,i}4-t)} + \frac{P_2}{1 + e^{P_5(P_{i,i}6-t)}, (2) i}$$

330 where the parameters P_1, P_2, \dots, P_6 determine the shape and asymmetry in
 331 the fitted double-logistic curve function (Bauer et al., 2017), while t indicates
 332 the consecutive day of year (DOY). The double-logistic function (2) was then
 333 fit using Matlab *lsqcurvefit* function, and the updated parameter values were
 334 used to interpolate EVI to a daily step (details are given in Supplementary
 335 Material, section B). Goodness of fit was assessed using root mean square
 336 error (RMSE) as a measure of deviation in the fitted model curve from the
 337 empirical data in a pixel series.

338 Statistical distributions of RMSE contained outliers exceeding the value
339 of 0.05, which corresponded largely to roads, berms and open water that
340 were not representative of wetland vegetation, but also in some cases -
341 vegetated areas with complex EVI trajectories where (2) was not sufficiently
342 applicable despite their similarity with PC1 or PC2. Several corrective
343 measures were applied to avoid immediately excluding such pixels from
344 phenological estimation (discussed in Supplementary Material section B,
345 Table S2 and Figure S3). These measures ranged from simpler steps, such as
346 re-fitting (2) after removing the observation with the largest residual, to
347 more complex measures, such as using a Fourier function as an alternative
348 harmonic regression model, or a combination of multiple strategies
349 (Supplementary Material section B, Table S2 and Figure S3). Such re-
350 assessments were more common with RapidEye data, especially at the MB
351 site where 69% RapidEye pixels retained after masking were fitted with the
352 double-logistic model, in contrast to 86-100% pixels for other site/sensor
353 combinations (Supplementary Table S3). Pixels where none of the strategies
354 improved model fitting were excluded from the analyses (Supplementary
355 Material section B).

356 Next, curvatures in the daily-interpolated EVI series were used to
357 estimate five metrics of phenological timing (Table 2; Supplementary Figure
358 S2; Supplementary Table S4): start and end of greening (SOG and EOG,
359 respectively) and senescence (SOS and EOS) and the duration (DUR) of the
360 growing season (Table 2; Supplementary Figure S2). For pixels fitted with

361 double-logistic model (1), these estimates were typically based on the local
362 minima and maxima of the 3rd derivative in the interpolated EVI series,
363 indicating changes in the rate of greenness dynamics at the onsets and end
364 times of greening and senescence (Gonsamo et al., 2013; Misra et al., 2016;
365 Tan et al., 2011). Depending on a site, such cases corresponded to 91-100%
366 fitted pixels with Landsat data and 52-77% pixels with RapidEye inputs
367 (Supplementary Table S3). In special cases where curvatures at the
368 beginning or end of the season were insufficiently captured by the data
369 series or an alternative fitting model was used (Supplementary Material
370 section B, Tables S2 and S4), local minima or maxima of the 2nd derivative
371 were admitted as the next closest approximation of phenological change
372 (Tan et al., 2011). Maximum greenness (MAXG, Table 2) was estimated from
373 the original pixel EVI values rather than predicted values, so that it could be
374 later compared with model RMSE. We expected that such a comparison
375 would help differentiate cases when modeling uncertainty resulted from
376 lower vegetation coverage and higher background exposure within a pixel
377 (Dronova and Taddeo, 2016) versus a disagreement between the
378 hypothetical fitted model and the spectral trajectory of pixels with high
379 vegetation coverage, and hence higher maximum greenness.

380 Importantly, the potential (dis)agreement of phenological metrics
381 between different satellite products may depend on multiple characteristics
382 of the product characteristics, including pixel size, specific timing of image
383 acquisitions and instrument characteristics, among others. Therefore, to

384 better understand the implications of varying spatial resolution on
385 phenological estimation and differences between Landsat and RapidEye
386 inputs, we additionally aggregated RapidEye data to a 30m pixel size
387 matching Landsat's resolution and evaluated the same phenological metrics
388 for 30m RapidEye-based pixels. We then compared median values and
389 statistical distributions of all phenological metrics within flux footprints
390 among the wetland sites and among the satellite inputs using non-
391 parametric Mood's median test (Mood, 1950) and Kruskal-Wallis distribution
392 test (Kruskal and Wallis, 1952), respectively.

393 **2.4. Relationships among satellite-based phenological** 394 **transitions and field-measured ecosystem properties**

395 To assess the potential relationships between the indicators of satellite-
396 detected phenology and ecosystem function, footprint-level mean and
397 median values of the four phenological timing metrics representing start and
398 end of greening and senescence phases (SOG, EOG, SOS and EOS) were
399 compared with 2016 time series of two field-based ecosystem variables:
400 spectral greenness indicator derived from midday digital photographs taken
401 by in situ phenocams (green chromatic coordinate, or GCC (Woebbecke et
402 al., 1995) and daily gap-filled net ecosystem exchange for CO₂ (NEE;
403 negative values indicate net ecosystem uptake (Chapin et al., 2006); gC-
404 CO₂m⁻²d⁻¹) from the flux towers. We subsequently fit the double-logistic
405 model (2) to each site's GCC and NEE time series to estimate the days of
406 year associated with their key seasonal transitions (curvatures). We then

407 regressed the days of the key transitions for GCC and NEE against the start
408 and end dates of greening and senescence estimated from the satellite-
409 based EVI and compared the slopes and intercepts of the regressions with
410 the 1:1 model (slope=1 and intercept=0) and between models using Landsat
411 versus RapidEye-based metrics. We acknowledge that such relationships
412 between EVI-based metrics and GCC should be interpreted with caution due
413 to the view angle differences between oblique phenocam images and
414 satellite data (Bolton et al., 2020; Vrieling et al., 2018). However, as field
415 datasets provide independent, high temporal frequency series with large
416 number of observations, they are useful for verifying the general agreement
417 between satellite-derived metrics and ground-based ecosystem transitions.

418 Finally, we compared satellite-measured EVI with water temperatures
419 summarized as daily averages for the image dates of each time series (Table
420 A1, Appendix) using field measurements from one location at each site, at
421 10-cm depth at MB and EE and 8-cm depth at WP. Water temperatures were
422 used here to represent potential effects of vegetation and canopy structure
423 on solar radiation transfer, and thus canopy microclimate (Eichelmann et al.,
424 2018; Rocha et al., 2008; Schile et al., 2013). We further examined whether
425 three wetland sites differed in the magnitude of their daily mean water
426 temperature during the growing season and in the slopes of EVI-water
427 temperature regressions for the dates of satellite image acquisitions.

428 **3. Results**

429 **3.1. Site and sensor differences in phenological timing**

430 Estimated phenological transition dates differed among wetland sites
431 (Figure 2a-d), with several notable features. First, WP, the site with the
432 highest vegetation and litter coverage (Table 1) showed pronounced delays
433 in greening compared to other wetlands (Figure 2a,b); however, specific
434 nature of these contrasts varied by satellite input. For Landsat, the median
435 start of greening (Figure 2a, Table A2, Appendix) was relatively synchronous
436 across the sites, with a 3-day difference between WP and MB ($p>0.1$), a 7-
437 day difference between WP and EE ($p>0.1$) and an 9-day earlier onset at EE
438 compared to MB ($p=0.003$). However, the median end of greening (Figure
439 2b, Table A2, Appendix) at MB was substantially earlier than at both WP (~73
440 days, $p<0.001$) and EE (~66 days, $p<0.001$), while the latter two sites
441 showed similar timing ($p>0.1$). In contrast, for RapidEye 5m inputs, both
442 median values and distributions of the start (Figure 2a) and the end (Figure
443 2b) of greening were significantly different across all site pairs ($p<0.001$,
444 Table A2, Appendix), but all of these median transition date estimates
445 similarly indicated greater (by 12-28 days) delay in greening at WP
446 compared to the other two sites. For RapidEye data aggregated to 30m pixel
447 size, however, only SOG was significantly different between all site pairs, but
448 not EOG (Table A2, Appendix).

449 These differences were also reflected in the spatial distribution of
450 greening dates, where the two most recently established sites, MB and EE,
451 showed a greater proportion of pixels with relatively earlier start and end of
452 greening compared to WP (Figures 3a-c for RapidEye-based start of greening

453 and Figure 3d-f for the end of greening). At the same time, however, the
454 agreement in greening transition dates between two satellite products was
455 not systematic among the sites (Figure 2a,b), showing the greatest disparity
456 for the more heterogeneous MB wetland where Landsat-based median end of
457 greening was 64 days earlier than RapidEye's at 5m resolution (Figure 2b).

458 FIGURE 2 ABOUT HERE

459 The timing of senescence also contrasted among the sites and satellite
460 inputs. For Landsat, both the start and the end of senescence were not
461 significantly different for any site pair (all p-values >0.1, Table A2,
462 Appendix). For RapidEye 5m input, however, all differences were significant
463 ($p < 0.001$), except the start of senescence between WP and EE ($p > 0.1$, Table
464 A2, Appendix). Two most vegetated sites WP and EE, again, showed the most
465 substantial delay in the start of senescence compared to MB (78 and 79
466 days, respectively, Figure 2c). In contrast, the RapidEye-based end of
467 senescence for 5m inputs differed among the sites by only 2-7 days,
468 comparable to 3-10 days for Landsat (Figure 2d). For RapidEye pixels
469 aggregated to 30m, only SOS significantly differed between MB and the
470 other two sites, while no site pairs significantly differed in EOS (Table A2,
471 Appendix).

472 Spatial variability in senescence dates also differed among three
473 wetlands, showing a more pronounced heterogeneity in the MB footprint
474 (Figure 3h and 3k) but also greater prevalence of late start and end of
475 senescence values at WP (Figure 3g and 3j) and EE (Figure 3i,l). Greater

476 overall variability of transition dates within the footprint of the more complex
477 MB wetland (Figures 3b,e,h,k) also highlighted the contrasts in phenology
478 between main vegetation patches and pixels representing water channels
479 and water-vegetation edges (visible as the interfaces between darker water
480 and lighter vegetation in reference images in Figure 3q). Water channel and
481 edge pixels were often characterized by later greening and earlier
482 senescence, which could result from differences in ecosystem elements and
483 vegetation contributing to greenness dynamics and contrasts in physical
484 environment (i.e., open water versus emergent patches).

485 FIGURE 3 ABOUT HERE

486 Median duration of the growing season (Figure 2e) was similar for all site
487 pairs for Landsat estimates ($p > 0.1$), but for RapidEye it was significantly
488 longer at EE and MB compared to WP (by 28 and 27 days, respectively,
489 $p < 0.001$ for each, Table A2, Appendix). After aggregating RapidEye pixels to
490 30m, all site pairs significantly differed in duration metric. Spatial variation in
491 per-pixel duration estimates (Figures 3m-o) suggested that the latter
492 differences resulted from presence of pixels with relatively early onset of
493 greening and relatively late senescence in both younger sites, which could
494 be areas where wetland vegetation was not obstructed by litter early in the
495 season. In contrast, most of the pixels at the oldest WP site (RapidEye
496 example in Figure 3m) corresponded to litter-laden patch interiors with a
497 relatively shorter growing season.

498 Finally, seasonal maximum of EVI significantly differed across the three
499 sites and their individual pairs regardless of the sensor (all p-values <0.05),
500 with the oldest WP site being the greenest, followed by the youngest EE as
501 the second greenest (Figure 2f). These patterns were largely consistent
502 among the two satellite datasets, although RapidEye-based estimates of
503 maximum greenness exhibited longer tails of high values in their
504 distributions compared to Landsat-based ones (Figure 2f). These tails were
505 likely due to the greater chance of capturing smaller clumps of green
506 vegetation cover with 5m pixels compared to 30m ones. For RapidEye
507 aggregated to 30m, maximum greenness significantly differed only between
508 MB and each of the other sites (Table A2, Appendix).

509 Among the satellite inputs, the lowest agreement in metric estimates
510 occurred at the most heterogeneous MB site where all except maximum
511 greenness significantly differed between Landsat and both RapidEye inputs
512 (Table A2, Appendix). For EE and WP, site-median differences between
513 Landsat and 5-m RapidEye metrics were within 1-14 days for SOG and EOG
514 (Figure 2a,b) and within 0-19 days for SOS, EOS and duration (Figure 2c,d,f).
515 In contrast, for MB, input differences were most pronounced for the
516 curvatures near peak growing season, showing a 64 day earlier EOG and 72-
517 day later SOS with Landsat (Figures 2b and 2c, respectively). Differences in
518 median SOG, EOS and DUR at MB were within 17-20 days, comparable to the
519 other two sites. However, most phenological metrics did not significantly
520 differ between Landsat and 30-m aggregated RapidEye except MAXG for WP

521 (Table A2, Appendix). Similarly, only three metrics significantly differed
522 between the original and aggregated RapidEye inputs: SOG and DUR for MB
523 and MAXG for WP (Table A2, Appendix), indicating no substantial effect of
524 RapidEye scaling on phenological estimation in more vegetated sites.

525 **3.2. Curve-fitting error and sensitivity to spatial resolution of** 526 **remote sensing data**

527 The median RMSE of the fitted phenological curve models did not
528 significantly differ among three wetlands for Landsat data ($p=0.074$; Figure
529 A1, Appendix). For RapidEye 5m input, median RMSE did not differ between
530 WP and MB ($p>0.1$) but was significantly lower at EE than at each of the
531 other two sites ($p<0.001$). When compared among the satellite inputs,
532 median RMSE was significantly ($p<0.001$) higher for the original 5m
533 RapidEye estimates compared to Landsat's and for the aggregated RapidEye
534 input for each site (Figure A1, Appendix). The proportion of pixels where
535 transition dates could be estimated using only 3rd derivative extrema of the
536 double-logistic model alone was also lower for RapidEye (52-77%;
537 Supplementary Table S3) compared to 91-100% for Landsat (Supplementary
538 Table S3).

539 Spatial distribution of RMSE within the flux footprints (Figure 4a,c,e,g,i,k)
540 indicated presence of local hotspots of higher fitting error that were also
541 more evident at higher spatial resolution of RapidEye (Figure 4a,e,i).
542 Comparing these local clusters of high RMSE to footprint aerial images
543 (Figure 3p-r) revealed that they were more common at the different types of

544 wetland vegetation edges: near roads and berms, visible in the WP footprint
545 (Figures 4a and 3p) and upper left portion of the MB footprint (Figures 4e and
546 3q), and near the vegetation-water interfaces in the lower left and central
547 parts of the EE footprint (Figures 4i and 3r) and parts of the MB footprint
548 (Figures 4e and 3q). Notably also, areas of higher RMSE often corresponded
549 to areas with higher maximum greenness (Figure 4b,f and j for RapidEye and
550 Figure 4d,h and l for Landsat). In fact, per-pixel RMSE significantly and
551 positively correlated with maximum EVI for nearly all site-sensor
552 combinations with p -value <0.001 and R^2 ranging between 0.32 and 0.66
553 (except for Landsat metrics at MB, $p>0.1$). In contrast, image regions with
554 lower RMSE (Figures 4b,f and j) often coincided with larger, contiguous
555 patches of wetland vegetation (Figures 3p-r).

556 FIGURE 4 ABOUT HERE

557 **3.3. Agreement between satellite-based phenological metrics** 558 **and field variables**

559 Both phenocam greenness (GCC) and net carbon exchange (NEE) followed
560 a seasonal trajectory similar to the double-logistic model of satellite-based
561 greenness for vegetation (Figures 5a and 5b, respectively). Both GCC and
562 NEE increased in magnitude during the first half of the year, stayed close to
563 their mid-year asymptotic values for a certain period of time and
564 subsequently reversed in late fall. However, specific shapes and timing of
565 these trajectories varied by site. The oldest site (WP) showed a later onset of
566 GCC greenness (\sim DOY 98) compared to MB and EE (\sim DOYs 69 and 51,

567 respectively); however, the end of greening for GCC was similar between two
568 more vegetated sites (DOYs 160 and 167 for EE and WP, respectively) than
569 for MB (DOY 117). The latter site also had lower maximum GCC and lower
570 magnitude of NEE (Figures 5a and 5b), which could be partially attributed to
571 field-detected increases in water salinity during 2015-2016 that may have
572 reduced the productivity and increased plant stress (Chamberlain et al.,
573 2019). The dynamics of NEE indicated an earlier onset for MB around DOY 68
574 compared to 85 and 99 at EE and WP, respectively, followed by an earlier
575 saturation near DOY 125, compared to 137 for EE and even more delayed
576 (192) for WP (Figure 5b). There were also notable site differences during the
577 senescence phase: for GCC, senescence at MB started approximately 102
578 and 140 days earlier than for EE and WP, respectively, though ended at a
579 similar time close to DOY 318. For NEE, the senescence phases were delayed
580 at WP and EE compared to MB by 17 and 19 days, respectively, at the onset
581 of senescence and by 31 and 45 days, respectively, at the end (Figure 5b).

582 Field-measured water-temperature (Figure 5c) showed a strong seasonal
583 change pattern for all sites, but differed in the rates of increase and
584 maximum values (Figure 5c). It was consistently the lowest at WP during the
585 main part of the growing season and similarly delayed in its seasonal
586 increase compared to the other two sites, as could be expected with a taller
587 canopy and presence of a litter layer affecting solar radiation transfer
588 through the canopy and canopy microclimate (Eichelmann et al., 2018;
589 Schile et al., 2013). In contrast, water temperature at MB site with greater

590 surface complexity and smaller vegetated patches was consistently the
591 highest among three wetlands, also showing an earlier seasonal increase
592 (Figure 5c).

593 FIGURE 5 ABOUT HERE

594 Satellite-estimated transition dates for greenness and senescence
595 strongly aligned with the DOYs of the key seasonal transitions (all $p < 0.001$)
596 from the field-measured phenocam greenness and NEE (Figure 6a,b). For
597 models comparing satellite and field GCC transition dates (Figure 5a),
598 regression slopes were not significantly different from 1, nor did they differ
599 between two satellite inputs (both $p > 0.1$, Table 3) despite the degree of
600 mismatch between satellite and phenocam fields of view (Knox et al., 2017).
601 However, for NEE transitions (Figure 5b) the slopes of regression with
602 Landsat and RapidEye's median DOYs were significantly greater than 1
603 ($p = 0.005$ and $p = 0.009$, respectively, Table 3). These patterns indicated the
604 tendency of satellite-based transitions to occur slightly ahead of the
605 corresponding changes in NEE early in the season, and slightly after NEE
606 changes late in the season (Figures 5b and 6b).

607 FIGURE 6 ABOUT HERE

608 TABLE 3 ABOUT HERE

609 Finally, water temperature for the dates of satellite image acquisitions
610 significantly and positively correlated with EVI of the corresponding remote
611 sensing series (Figure 7a,b). The slopes of these relationships did not differ
612 between satellite inputs for any of the sites ($p > 0.1$ for all slope

613 comparisons). However, for both Landsat (Figure 7a) and RapidEye (Figure
614 7b), the slope of EVI-water temperature relationship for WP was significantly
615 steeper than for either MB ($p=0.006$ and $p=0.001$ for Landsat and RapidEye,
616 respectively) or EE ($p=0.026$ and $p=0.023$ for Landsat and RapidEye,
617 respectively), and did not differ between the latter ($p>0.1$ for each). In turn,
618 water temperatures corresponding to the dates of estimated SOG and EOG
619 for each satellite series significantly differed ($p<0.001$) between three sites.
620 These temperatures, however, were all lower for WP, indicating cooler sub-
621 canopy conditions at the onset and the end of greening.

622 FIGURE 7 ABOUT HERE

623 **4. Discussion**

624 **4.1. Spatial phenological heterogeneity as the indicator of** 625 **restoration outcomes**

626 As ecological restoration efforts continue expanding, the need to
627 understand how their novel outcomes contribute to ecosystem management
628 and conservation becomes ever more urgent (Matthews et al., 2009; Mitsch
629 et al., 2013; Villa and Bernal, 2018). Our analysis of satellite-based
630 phenological metrics across three restored wetlands in California's Delta
631 region corroborates the unique potential of remote sensing to help develop
632 this understanding via repeated cost-effective observations. Our findings
633 also highlight the need for more spatially explicit phenological analyses, for
634 two important reasons. First, the timing of phenological transitions appears
635 to vary substantially among wetland sites with similar geographic setting,

636 vegetation and hydrology but contrasting surface composition and canopy
637 structure. This limits the representativeness of aggregated single-site data
638 and calls for individual, spatially explicit site-level observations which are
639 becoming increasingly feasible (Csillik et al., 2019; Gorelick et al., 2017;
640 Tóth, 2018; Woodcock et al., 2020). Second, we find that the agreement in
641 phenological indicators between satellite inputs of different spatial resolution
642 may also vary among wetlands with different amount and configuration of
643 vegetation cover. Such differences in spatial heterogeneity and phenology
644 may further contribute to the functional contrasts among sites, as suggested
645 by the agreement between satellite-detected EVI transition dates and the
646 timing of in situ measured phenocam greenness and CO₂ exchange (Figure
647 5).

648 From the remote sensor's perspective, two main factors likely contributed
649 to heterogeneity of phenological metrics and challenges in their estimation:
650 wetland surface and plant composition (Vrieling et al., 2018) and the effects
651 of non-photosynthetic plant matter on canopy structure, radiative transfer
652 and microclimate (Dronova and Taddeo, 2016; Farrer and Goldberg, 2009;
653 Rocha et al., 2008; Schile et al., 2013). Despite relatively low diversity of the
654 emergent vascular plants in these wetlands, some non-dominant species
655 could have distinct seasonality and form local patches large enough to
656 influence pixel-level EVI dynamics. For example, portions of the flux
657 footprints near roads and berms included grasses, herbs and sometimes
658 woody species, while some of the open-water areas had floating aquatic

659 vegetation. Both types of such locations (i.e., berms and open water areas;
660 Figure 3p-r) differed in phenological timing from the reed-dominated wetland
661 patches, particularly for the start of greening (Figure 3a-c) and duration
662 (Figure 3m-o).

663 In turn, the 3-D complexity of plant canopies and presence of dead
664 biomass (Dronova and Taddeo, 2016; Rocha et al., 2008; Rocha and
665 Goulden, 2009; Tóth, 2018) likely contributed to the wide range of start and
666 end dates of phenological phases observed even within the larger wetland
667 vegetation patches (Figure 3p-r). Although full understanding of such effects
668 is difficult without spatially explicit information on canopy structure, the
669 following evidence suggests the importance of both horizontal and vertical
670 configuration of vegetation in these patterns. First, as expected,
671 phenological differences among wetland sites closely resonated with
672 differences in their spatial heterogeneity and configuration. Greater greening
673 delays within the oldest and the youngest wetlands, WP and EE (Figure 2a,b),
674 were consistent with their greater plant coverage, patch size, canopy height
675 and canopy-to-litter height proportion (Table 1). In contrast, less contiguous
676 plant coverage together with smaller patch size and greater shape index at
677 MB site (Figure 3r, Table 1) would imply a greater availability of fine-scale
678 edge spaces both at the perimeters and inside the patches, where green
679 vegetation may have greater access to light and become visible to remote
680 sensors earlier compared to larger, contiguous patches of the other two sites
681 (Dronova and Taddeo, 2016).

682 Second, the general agreement in the timing of remotely sensed
683 phenological metrics and site-measured ecosystem processes indicates that
684 phenological variability was not merely an optical artifact of litter obscuring
685 green vegetation from the sensors' view, but rather the outcome of more
686 complex feedbacks among canopy structure, microclimate and plant function
687 (Eichelmann et al., 2018; Hemes et al., 2018). Regardless of the input
688 satellite product, delays in greening were accompanied by delays in seasonal
689 enhancement of CO₂ uptake (Figures 5a,b and 6b) and phenocam greenness,
690 which had been earlier shown to positively correlate with gross primary
691 productivity at MB and WP (Knox et al., 2017). Presence of litter likely
692 mediated these relationships via reduced solar energy to young short
693 vegetation early in the season, and via its broader effects on sub-canopy
694 microclimate and evapotranspiration (Eichelmann et al., 2018; Goulden et
695 al., 2007; Hemes et al., 2018; Rejšková et al., 2012). Although here we
696 cannot directly validate such causal effects due to the lack of spatially
697 explicit data on site-level litter distribution, microclimatic contrasts among
698 three wetlands throughout the study period were consistent with this
699 assertion. In particular, lower water temperatures and their smaller change
700 change in unit greenness (Figure 7a,b) at WP and EE with larger litter-laden
701 vegetation patches could contribute to their stronger greenness delay
702 (Figures 2b and 5c) compared to MB due to potential inhibition of plant and
703 microbial metabolism early in the season.

704 Some of the deviations from a 1:1 agreement between satellite-derived
705 phenological transition dates and those estimated from GCC and NEE series
706 (Figure 6a,b) could also result from the differences in ecosystem sampling
707 between satellite and ground instruments. A recent continental-scale
708 analysis of ecosystem phenology combining Landsat-8 and Sentinel-2
709 imagery (Bolton et al., 2020) has noted stronger disagreements between
710 satellite and phenocam estimates in more heterogeneous systems as well as
711 landscapes with sparser vegetation cover. Applying this evidence to restored
712 deciduous marshes may suggest that, similar to our findings, the agreement
713 among different remote sensing systems should vary both with the degree of
714 surface complexity at a given post-restoration stage, and possibly even with
715 season, due to differences in plant density and canopy structure. These
716 considerations, again, point to the difficulties in generalizing ecosystem
717 cycles among heterogeneous areas (Eichelmann et al., 2018; Goulden et al.,
718 2007; Larsen and Harvey, 2011; Rocha et al., 2008; Schile et al., 2013) and
719 underscore the need for more spatially explicit phenological analyses at the
720 site level, which are not feasible with oblique single-location phenocam
721 images alone (Bolton et al., 2020; Vrieling et al., 2018).

722 **4.2. The implications of spatial resolution and frequency of** 723 **remote sensing data**

724 Our findings also show that heterogeneity of vegetation in relation to
725 spatial resolution of a remote sensing product is a critical consideration in
726 selecting the input data for phenological analyses. Smaller pixels enable

727 more accurate representation of vegetation patch structure and floristic
728 components as a potential contributor to site-level ecosystem function
729 (Eichelmann et al., 2018; Matthes et al., 2014; McNicol et al., 2017). For
730 example, stronger agreement between RapidEye-based phenological
731 transitions with those of field GCC and NEE (Figure 6) compared to Landsat-
732 based ones could be in part due to better separation of vegetation and water
733 and thus lower likelihood of mixed-cover pixels where water may attenuate
734 vegetation signals (Kearney et al., 2009). As a result, 5m RapidEye pixels
735 retained after masking would be expected to more closely resemble green
736 vegetation as seen by oblique-looking phenocams than 30m Landsat pixels
737 with a greater chance of including background water signals (Dronova and
738 Taddeo 2016). In terms of spatial representation of the footprints, the cost of
739 “losing” a pixel due to noise and inconsistency with the phenological model
740 is obviously higher with coarser-resolution Landsat data, since there are
741 fewer overall pixels and each covers a larger area than a RapidEye’s pixel, as
742 was especially evident at the EE site (Supplementary Tables S1 and S3).

743 However, in this study benefits of the high-resolution dataset also came at
744 the cost of somewhat higher model fitting error (Figures A1 (Appendix) and
745 4) and greater diversity of pixel-level trajectories that were not always easy
746 to accommodate by the standard mathematical functions (Supplementary
747 Material section B, Tables S2 and S4). These challenges likely contributed to
748 greater model RMSE with 5m RapidEye inputs (Appendix Figure A1) and to
749 the positive association between RMSE and maximum EVI, also more evident

750 with RapidEye data (Figure 4). These patterns likely reflected the potential of
751 smaller pixels to capture more nuanced and localized seasonal variation in
752 canopy reflectance spectra, affecting seasonal change in EVI. For example,
753 duration and consistency of the phenological phases with higher greenness
754 could be affected by various events and processes such as flowering,
755 disturbance, mortality, or changes in green leaf orientation (e.g., Bolton et
756 al., 2020; Ryu et al., 2010; Sonnentag et al., 2011), making per-pixel EVI
757 trajectories more complex than in a hypothetical model (Figure S2,
758 Supplementary Material).

759 Together, these results highlight an important tradeoff between two
760 aspects of phenological complexity in heterogeneous systems: coarser
761 spatial resolution increases the chance of mixed pixels where phenological
762 trajectory may be complicated by the seasonality of both vegetated and non-
763 vegetated components, while higher resolution may accentuate local
764 phenological and spectral variability even for exclusively vegetated pixels,
765 posing challenges to traditional curve-fitting approaches. Smoothing the
766 satellite-derived EVI time series using moving time windows might also be
767 impractical if there are substantial gaps between image acquisition dates, as
768 this might reduce the accuracy of estimated transitions. Optimizing the
769 choice of remote sensing products thus should weigh the relative importance
770 of spatial accuracy in representing landscape elements (e.g., patches) versus
771 the ratio of temporal noise relative to phenologically relevant signal, both of
772 which may increase with smaller pixel size. These findings also highlight the

773 shortcomings of phenological estimation approaches developed in “upland”
774 terrestrial ecosystems within complex wetland environments and call for
775 more rigorous wetland-specific assessments which have been scarce to date
776 (Mo et al., 2015; Vrieling et al., 2018).

777 Finally, the agreement in the estimated timing of greening and
778 senescence between satellite inputs may also depend on their image
779 acquisition dates (Bolton et al., 2020; Melaas et al., 2016, 2013; Vrieling et
780 al., 2018). For our single-year study this issue was not a major concern, as
781 indicated by relatively high temporal frequency of both datasets (Table A1,
782 Appendix) and the general agreement of the satellite-derived DOYs of
783 greening and senescence with the phenology of field-based phenocam GCC
784 greenness (Figure 6a). However, disparities in phenological metrics between
785 Landsat and both original and aggregated RapidEye inputs for the most
786 heterogeneous MB site (Table A2, Appendix) suggest that phenological
787 analyses might be more sensitive to both sensor-specific spatial resolution
788 and image timing in landscapes with greater complexity and phenological
789 variability (Tóth, 2018; Vrieling et al., 2018). In general, less frequent image
790 series can be more strongly impacted by cloudy conditions leading to
791 prolonged gaps between usable dates. From this perspective, greater
792 frequencies of RapidEye and other new platforms such as Sentinel-2 (Bolton
793 et al., 2020; Claverie et al., 2018; Vrieling et al., 2018) become an obvious
794 advantage over Landsat’s 8-16 day intervals between acquisitions even
795 during cloud-free seasons. These considerations also argue for a wider

796 adoption of cost-effective, high temporal frequency phenological validation
797 and gap-filling strategies, such as in situ phenocam systems (Knox et al.,
798 2017; Richardson et al., 2018; Sonnentag et al., 2012) and unmanned
799 vehicles (Tóth, 2018).

800 **4.3. Future research needs**

801 Collectively, our findings suggest that phenological indicators derived
802 from high- and moderate-resolution passive remote sensing images can be
803 sensitive to spatio-temporal heterogeneity of ecosystems and the potential
804 links between vegetation structure and function targeted by restoration and
805 management (Matthes et al., 2014; McNicol et al., 2017). However, a more
806 in-depth interpretation of such couplings ultimately requires spatially explicit
807 information on 3-D canopy structure which could be characterized using
808 multi-angular spectral reflectance (Hilker et al., 2011) and/or active remote
809 sensing such as lidar (LaRue et al., 2018). At present, lidar data are not
810 systematically acquired in our study area, and high cost of such data
811 collection over large regions generally limits their use in ecosystem
812 monitoring (Taddeo and Dronova, 2019). However, where available, active
813 remote sensing data could facilitate more in-depth studies of the role of
814 canopy structure in phenological variability. Employing such instruments on
815 the unmanned platforms (Bekaert et al., 2019; Sharma et al., 2016; Tóth,
816 2018) could be especially useful in complex systems to develop such an
817 understanding in a cost-effective and spatially explicit way.

818 Future research should also more closely investigate the role of site-

819 specific environmental conditions in phenological contrasts among wetlands
820 with similar vegetation and hydrology. In addition to patch configuration and
821 3-D structure, phenological patterns could be also associated with less well
822 known variation in wetland soil and water column characteristics
823 (Chamberlain et al., 2018; Franz et al., 2016; Minke et al., 2016; Smesrud et
824 al., 2014; Strachan et al., 2015). In particular, the correspondence of greater
825 phenological delay with high maximum greenness (Figure 2) in the sites with
826 higher LAI, canopy height (Table 1) and NEE (Figure 5b) presents an
827 interesting paradox to examine in the future. One of the possible reasons for
828 this association could be the effects of site-specific soil properties, salinity
829 and litter on nutrient status (Chamberlain et al., 2018; Farrer and Goldberg,
830 2009; Tóth, 2018), potentially affecting spectral reflectance via both the
831 amount and chemistry of green foliage (Byrd et al., 2014). For instance,
832 salinization of wetland soils at the MB site during the California drought of
833 2011-2017 reduced its annual gross ecosystem productivity compared to
834 WP, consistent with our observed contrasts in maximum greenness between
835 these sites (Chamberlain et al., 2018). Similarly, a study of phenological
836 variability in freshwater *Phragmites* stands at Lake Balaton, Hungary (Tóth,
837 2018) reported a stronger sensitivity of phenological variation to sediment
838 texture and chemical properties than to air and water temperature.
839 Alternatively, greater litter accumulation could be hypothesized to enhance
840 site quality (Lenssen et al., 1999) and protect the reed seedlings in patch
841 interior from wind and water-related disturbance (Zhang and Wang, 2016),

842 which, again, could be tested more explicitly via experimental studies.

843 Finally, to better understand the implications of the coupled structure-
844 function relationships for restoration outcomes, future studies should
845 investigate the inter-annual variability in wetland phenology using longer-
846 term satellite product archives, such as Landsat's, at least in areas with
847 sufficiently cloud-free time series. Such multi-year assessments could
848 elucidate the potential cycles in spectral contributions of litter (Anderson et
849 al., 2016; Rocha et al., 2008) and the role of these cycles in stability and
850 resilience of the ecosystem functions in response to climatic anomalies
851 (Rocha and Goulden, 2010) or pest outbreaks. Increasing availability of
852 higher-resolution remote sensing datasets capable of characterizing
853 ecosystem heterogeneity and phenological dynamics (e.g., Sentinel-2, Planet
854 Lab products) expands this critical new frontier for more continuous
855 monitoring of ecosystem function (Bolton et al., 2020; Claverie et al., 2018;
856 Matthes et al., 2014; Vrieling et al., 2018). Ultimately, the knowledge derived
857 from comprehensive analyses of richer remote sensing series would also
858 support the upscaling of ecosystem function and associated ecological
859 benefits from local sites to regional scales and similar efforts in other
860 locations.

861 **5. Conclusions**

862 Remote sensing products are increasingly used to characterize
863 phenological transitions of ecosystems and their functional dynamics;
864 however, the sensitivity of such assessments to local vegetation structure

865 and scale of remote sensing data is still not universally understood. This gap
866 is especially evident in spatially heterogeneous systems such as wetlands,
867 where remotely sensed vegetation indicators may depend on local mixing of
868 plants and non-vegetated surfaces and the complexity of canopy structure at
869 a given image resolution, which might further vary in the course of ecological
870 restoration or succession. Understanding the implications of heterogeneity
871 on remotely sensed phenological indicators thus becomes critical for
872 interpreting links between plant structure and function and their sensitivity
873 to management and restoration treatments.

874 Our study of three restored wetlands in California, USA finds that even
875 under similar floristic composition and geographic setting, wetlands may
876 differ in remotely sensed phenological characteristics in accordance with
877 their contrasts in vegetation coverage and structure. Such differences are
878 especially evident in variable length and timing of the greening phase which
879 can be more delayed in areas with larger vegetation patches and greater
880 accumulation of canopy litter. The consistency between site-level remotely
881 sensed phenological metrics and field-based changes in eddy covariance
882 NEE for CO₂ as well as phenocam greenness suggests that such delays may
883 reflect the local effects of litter on canopy radiative transfer, water
884 temperatures and microclimate. A more in-depth investigation of this
885 assertion would benefit from incorporating spatially explicit information on
886 local canopy structure, e.g., from lidar instruments.

887 We also show that both the local spatial variability in phenological metrics
888 and the disagreement in their estimation between two satellite inputs tended
889 to be higher in wetlands with more heterogeneous surface configuration. We
890 also find that the uncertainty in fitting standard phenological models pixel-
891 level greenness series increased with greater spatial resolution, likely due to
892 greater sensitivity of smaller pixels to local-scale variation in phenological
893 patterns within vegetation patches. Such tradeoffs between the benefits of
894 higher spatial resolution and the analysis uncertainty raise an important
895 question on which spatial and temporal scales most effectively represent the
896 links between vegetation structure and function, particularly in complex
897 systems such as restored wetlands. With the increasing interest in multi-
898 sensor data integration efforts and higher-resolution phenological products,
899 this question highlights an important research need to inform future remote
900 sensing uses in monitoring, modeling and up-scaling of ecosystem function
901 and restoration outcomes.

902 **Acknowledgements**

903 We thank PlanetLabs Education and Research program for the access to
904 RapidEye satellite imagery used in this study. Funding for the wetland data
905 collection and processing from AmeriFlux core sites was provided by the U.S.
906 Department of Energy's Office of Science for the AmeriFlux Management
907 Project under the Contract No. DE-AC02-05CH11231, and by California
908 Department of Water Resources through a contract from the California
909 Department of Fish and Wildlife, Award number 4600011240. Measurements

910 of wetland site patch configuration were conducted in the project supported
911 by the California Sea Grant Delta Science Award R/SF-71. Kuno Kasak's
912 collaboration was supported by the Baltic-American Freedom Foundation and
913 Estonian Research Council (grants no. PUTJD715 and PRG352).

914 **References**

- 915 Anderson, F.E., Bergamaschi, B., Sturtevant, C., Knox, S., Hastings, L.,
916 Windham-Myers, L., Detto, M., Hestir, E.L., Drexler, J., Miller, R.L.,
917 Matthes, J.H., Verfaillie, J., Baldocchi, D., Snyder, R.L., Fujii, R., 2016.
918 Variation of energy and carbon fluxes from a restored temperate
919 freshwater wetland and implications for carbon market verification
920 protocols: Variability in Wetland Fluxes. *J. Geophys. Res.*
921 *Biogeosciences* 121, 777–795. <https://doi.org/10.1002/2015JG003083>
922 Baldocchi, D., Hicks, B., Meyers, T., 1988. Measuring biosphere-atmosphere
923 exchanges of biologically related gases with micrometeorological
924 methods. *Ecology* 69, 1331–1340. <https://doi.org/10.2307/1941631>
925 Bauer, L.G.M., Hametner, B., Mayer, C.C., Wassertheurer, S., 2017.
926 Mathematical Wave Fitting Models for the Quantification of the Diurnal
927 Profile and Variability of Pulse Wave Analysis Parameters. *SNE Simul.*
928 *Notes Eur.* 27, 153–160. <https://doi.org/10.11128/sne.27.tn.10386>
929 Bekaert, D.P.S., Jones, C.E., An, K., Huang, M.-H., 2019. Exploiting UAVSAR
930 for a comprehensive analysis of subsidence in the Sacramento Delta.
931 *Remote Sens. Environ.* 220, 124–134.
932 <https://doi.org/10.1016/j.rse.2018.10.023>
933 Bolton, D.K., Gray, J.M., Melaas, E.K., Moon, M., Eklundh, L., Friedl, M.A.,
934 2020. Continental-scale land surface phenology from harmonized
935 Landsat 8 and Sentinel-2 imagery. *Remote Sensing of Environment*
936 240, 111685. <https://doi.org/10.1016/j.rse.2020.111685>
937 Butterfield, H.S., Malmstroem, C.M., 2009. The effects of phenology on
938 indirect measures of aboveground biomass in annual grasses. *Int. J.*
939 *Remote Sens.* 30, 3133–3146.
940 <https://doi.org/10.1080/01431160802558774>
941 Byrd, K.B., O'Connell, J.L., Di Tommaso, S., Kelly, M., 2014. Evaluation of
942 sensor types and environmental controls on mapping biomass of
943 coastal marsh emergent vegetation. *Remote Sens. Environ.* 149, 166–
944 180. <https://doi.org/10.1016/j.rse.2014.04.003>
945 Chamberlain, S.D., Anthony, T.L., Silver, W.L., Eichelmann, E., Hemes, K.S.,
946 Oikawa, P.Y., Sturtevant, C., Szutu, D.J., Verfaillie, J.G., Baldocchi, D.D.,
947 2018. Soil properties and sediment accretion modulate methane fluxes
948 from restored wetlands. *Glob. Change Biol.* 24, 4107–4121.
949 <https://doi.org/10.1111/gcb.14124>

950 Chamberlain, S.D., Hemes, K.S., Eichelmann, E., Szutu, D.J., Verfaillie, J.G.,
951 Baldocchi, D.D., 2019. Effect of Drought-Induced Salinization on
952 Wetland Methane Emissions, Gross Ecosystem Productivity, and Their
953 Interactions. *Ecosystems*. <https://doi.org/10.1007/s10021-019-00430-5>

954 Chapin, F.S., Woodwell, G.M., Randerson, J.T., Rastetter, E.B., Lovett, G.M.,
955 Baldocchi, D.D., Clark, D.A., Harmon, M.E., Schimel, D.S., Valentini, R.,
956 Wirth, C., Aber, J.D., Cole, J.J., Goulden, M.L., Harden, J.W., Heimann,
957 M., Howarth, R.W., Matson, P.A., McGuire, A.D., Melillo, J.M., Mooney,
958 H.A., Neff, J.C., Houghton, R.A., Pace, M.L., Ryan, M.G., Running, S.W.,
959 Sala, O.E., Schlesinger, W.H., Schulze, E.-D., 2006. Reconciling Carbon-
960 cycle Concepts, Terminology, and Methods. *Ecosystems* 9, 1041-1050.
961 <https://doi.org/10.1007/s10021-005-0105-7>

962 Chapple, D., Dronova, I., 2017. Vegetation Development in a Tidal Marsh
963 Restoration Project during a Historic Drought: A Remote Sensing
964 Approach. *Front. Mar. Sci.* 4. <https://doi.org/10.3389/fmars.2017.00243>

965 Chu, H., Chen, J., Gottgens, J.F., Ouyang, Z., John, R., Czajkowski, K., Becker,
966 R., 2014. Net ecosystem methane and carbon dioxide exchanges in a
967 Lake Erie coastal marsh and a nearby cropland: CH₄ and CO₂ fluxes in
968 a freshwater marsh. *J. Geophys. Res. Biogeosciences* 119, 722-740.
969 <https://doi.org/10.1002/2013JG002520>

970 Chu, H., Gottgens, J.F., Chen, J., Sun, G., Desai, A.R., Ouyang, Z., Shao, C.,
971 Czajkowski, K., 2015. Climatic variability, hydrologic anomaly, and
972 methane emission can turn productive freshwater marshes into net
973 carbon sources. *Glob. Change Biol.* 21, 1165-1181.
974 <https://doi.org/10.1111/gcb.12760>

975 Claverie, M., Ju, J., Masek, J.G., Dungan, J.L., Vermote, E.F., Roger, J.-C.,
976 Skakun, S.V., Justice, C., 2018. The Harmonized Landsat and Sentinel-2
977 surface reflectance data set. *Remote Sens. Environ.* 219, 145-161.
978 <https://doi.org/10.1016/j.rse.2018.09.002>

979 Csillik, O., Kumar, P., Mascaro, J., O'Shea, T., Asner, G.P., 2019. Monitoring
980 tropical forest carbon stocks and emissions using Planet satellite data.
981 *Sci. Rep.* 9, 17831. <https://doi.org/10.1038/s41598-019-54386-6>

982 Detto, M., Montaldo, N., Albertson, J.D., Mancini, M., Katul, G., 2006. Soil
983 moisture and vegetation controls on evapotranspiration in a
984 heterogeneous Mediterranean ecosystem on Sardinia, Italy:
985 EVAPOTRANSPIRATION IN MEDITERRANEAN ECOSYSTEM. *Water*
986 *Resour. Res.* 42. <https://doi.org/10.1029/2005WR004693>

987 Deverel, S., 2015. Evolution of Arability and Land Use, Sacramento-San
988 Joaquin Delta, California. *San Franc. Estuary Watershed Sci.* 13, 1-34.

989 Deverel, S., Leighton, D., HydroFocus, Inc., Lucero, C., HydroFocus, Inc.,
990 Ingrum, T., HydroFocus, Inc., 2017. Simulation of Subsidence Mitigation
991 Effects on Island Drain Flow, Seepage, and Organic Carbon Loads on
992 Subsided Islands Sacramento-San Joaquin Delta. *San Franc. Estuary*
993 *Watershed Sci.* 15. <https://doi.org/10.15447/sfews.2017v15iss4art2>

994 Deverel, S.J., Leighton, D.A., Hydrofocus, Inc., 2010. Historic, Recent, and
995 Future Subsidence, Sacramento-San Joaquin Delta, California, USA. *San*

996 Franc. Estuary Watershed Sci. 8.
997 <https://doi.org/10.15447/sfews.2010v8iss2art1>
998 Dronova, I., Bergen, K.M., Ellsworth, D.S., 2011. Forest Canopy Properties
999 and Variation in Aboveground Net Primary Production over Upper Great
1000 Lakes Landscapes. *Ecosystems* 14, 865–879.
1001 <https://doi.org/10.1007/s10021-011-9451-9>
1002 Dronova, I., Taddeo, S., 2016. Canopy Leaf Area Index in Non-Forested
1003 Marshes of the California Delta. *Wetlands* 36, 705–716. [https://doi.org/](https://doi.org/10.1007/s13157-016-0780-5)
1004 [10.1007/s13157-016-0780-5](https://doi.org/10.1007/s13157-016-0780-5)
1005 Eichelmann, E., Hemes, K.S., Knox, S.H., Oikawa, P.Y., Chamberlain, S.D.,
1006 Sturtevant, C., Verfaillie, J., Baldocchi, D.D., 2018. The effect of land
1007 cover type and structure on evapotranspiration from agricultural and
1008 wetland sites in the Sacramento–San Joaquin River Delta, California.
1009 *Agric. For. Meteorol.* 256–257, 179–195.
1010 <https://doi.org/10.1016/j.agrformet.2018.03.007>
1011 Farrer, E.C., Goldberg, D.E., 2009. Litter drives ecosystem and plant
1012 community changes in cattail invasion. *Ecol. Appl.* 19, 398–412. [https://](https://doi.org/10.1890/08-0485.1)
1013 doi.org/10.1890/08-0485.1
1014 Flanagan, N.E., Richardson, C.J., Ho, M., 2015. Connecting differential
1015 responses of native and invasive riparian plants to climate change and
1016 environmental alteration. *Ecol. Appl.* 25, 753–767.
1017 <https://doi.org/10.1890/14-0767.1>
1018 Franz, D., Koebsch, F., Larmanou, E., Augustin, J., Sachs, T., 2016. High net
1019 CO₂ and CH₄ release at
1020 a eutrophic shallow lake on a formerly drained fen. *Biogeosciences* 13,
1021 3051–3070. <https://doi.org/10.5194/bg-13-3051-2016>
1022 Friedl, M.A., Gray, J.M., Melaas, E.K., Richardson, A.D., Hufkens, K., Keenan,
1023 T.F., Bailey, A., O’Keefe, J., 2014. A tale of two springs: using recent
1024 climate anomalies to characterize the sensitivity of temperate forest
1025 phenology to climate change. *Environ. Res. Lett.* 9, 054006.
1026 <https://doi.org/10.1088/1748-9326/9/5/054006>
1027 Gonsamo, A., Chen, J.M., D’Odorico, P., 2013. Deriving land surface
1028 phenology indicators from CO₂ eddy covariance measurements. *Ecol.*
1029 *Indic.* 29, 203–207. <https://doi.org/10.1016/j.ecolind.2012.12.026>
1030 Gorelick, N., Hancher, M., Dixon, M., Ilyushchenko, S., Thau, D., Moore, R.,
1031 2017. Google Earth Engine: Planetary-scale geospatial analysis for
1032 everyone. *Remote Sens. Environ.* 202, 18–27.
1033 <https://doi.org/10.1016/j.rse.2017.06.031>
1034 Goulden, M.L., Litvak, M., Miller, S.D., 2007. Factors that control Typha marsh
1035 evapotranspiration. *Aquat. Bot.* 86, 97–106.
1036 <https://doi.org/10.1016/j.aquabot.2006.09.005>
1037 Gu, L., Post, W.M., Baldocchi, D., Andy Black, T., Verma, S.B., Vesala, T.,
1038 Wofsy, S.C., 2003. Phenology of Vegetation Photosynthesis, in:
1039 Schwartz, M.D. (Ed.), *Phenology: An Integrative Environmental Science*.
1040 Springer Netherlands, Dordrecht, pp. 467–485.
1041 https://doi.org/10.1007/978-94-007-0632-3_29

1042 Head, G.A., Lukoshkova, E.V., Mayorov, D.N., van den Buuse, M., 2004. Non-
1043 symmetrical double-logistic analysis of 24-h blood pressure recordings
1044 in normotensive and hypertensive rats: *J. Hypertens.* 22, 2075–2085.
1045 <https://doi.org/10.1097/00004872-200411000-00008>

1046 Hemes, K.S., Chamberlain, S.D., Eichelmann, E., Anthony, T., Valach, A.,
1047 Kasak, K., Szutu, D., Verfaillie, J., Silver, W.L., Baldocchi, D.D., 2019.
1048 Assessing the carbon and climate benefit of restoring degraded
1049 agricultural peat soils to managed wetlands. *Agric. For. Meteorol.* 268,
1050 202–214. <https://doi.org/10.1016/j.agrformet.2019.01.017>

1051 Hemes, K.S., Eichelmann, E., Chamberlain, S.D., Knox, S.H., Oikawa, P.Y.,
1052 Sturtevant, C., Verfaillie, J., Szutu, D., Baldocchi, D.D., 2018. A Unique
1053 Combination of Aerodynamic and Surface Properties Contribute to
1054 Surface Cooling in Restored Wetlands of the Sacramento-San Joaquin
1055 Delta, California. *J. Geophys. Res. Biogeosciences* 123, 2072–2090.
1056 <https://doi.org/10.1029/2018JG004494>

1057 Hilker, T., Gitelson, A., Coops, N.C., Hall, F.G., Black, T.A., 2011. Tracking
1058 plant physiological properties from multi-angular tower-based remote
1059 sensing. *Oecologia* 165, 865–876. <https://doi.org/10.1007/s00442-010-1901-0>

1061 Hill, D.T., Payton, J.D., 2000. Effect of plant fill ratio on water temperature in
1062 constructed wetlands1This work was supported by the Alabama
1063 Agricultural Experiment Station (AAES) under Regional Research
1064 Project S-275 and by the USDA-NRCS under Cooperative Agreement
1065 No. 68-4104-2-18. It is designated as Journal Series No. 2-985925 by
1066 the AAES.1. *Bioresour. Technol.* 71, 283–289.
1067 [https://doi.org/10.1016/S0960-8524\(99\)90071-8](https://doi.org/10.1016/S0960-8524(99)90071-8)

1068 Hsieh, C.-I., Katul, G., Chi, T., 2000. An approximate analytical model for
1069 footprint estimation of scalar fluxes in thermally stratified atmospheric
1070 flows. *Adv. Water Resour.* 23, 765–772. [https://doi.org/10.1016/S0309-1708\(99\)00042-1](https://doi.org/10.1016/S0309-1708(99)00042-1)

1072 Huesca, M., Merino-de-Miguel, S., Eklundh, L., Litago, J., Cicuendez, V.,
1073 Rodriguez-Rastrero, M., Ustin, S.L., Palacios-Orueta, A., 2015.
1074 Ecosystem functional assessment based on the “optical type” concept
1075 and self-similarity patterns: An application using MODIS-NDVI time
1076 series autocorrelation. *Int. J. Appl. Earth Obs. Geoinformation* 43, 132–
1077 148. <https://doi.org/10.1016/j.jag.2015.04.008>

1078 Huete, A., Didan, K., Miura, T., Rodriguez, E.P., Gao, X., Ferreira, L.G., 2002.
1079 Overview of the radiometric and biophysical performance of the MODIS
1080 vegetation indices. *Remote Sens. Environ.* 83, 195–213. [https://doi.org/10.1016/S0034-4257\(02\)00096-2](https://doi.org/10.1016/S0034-4257(02)00096-2)

1082 Hufkens, K., Friedl, M., Sonnentag, O., Braswell, B.H., Milliman, T.,
1083 Richardson, A.D., 2012. Linking near-surface and satellite remote
1084 sensing measurements of deciduous broadleaf forest phenology.
1085 *Remote Sens. Environ.* 117, 307–321.
1086 <https://doi.org/10.1016/j.rse.2011.10.006>

1087 Keine, C., 2020. Moods Median Test
1088 (<https://github.com/ChristianKeine/Moods-Mediantest>), GitHub.
1089 Retrieved August 16, 2020.

1090 Kearney, M.S., Stutzer, D., Turpie, K., Stevenson, J.C., 2009. The Effects of
1091 Tidal Inundation on the Reflectance Characteristics of Coastal Marsh
1092 Vegetation. *J. Coast. Res.* 25, 1177–1186. [https://doi.org/10.2112/08-](https://doi.org/10.2112/08-1080.1)
1093 [1080.1](https://doi.org/10.2112/08-1080.1)

1094 Keenan, T.F., Baker, I., Barr, A., Ciais, P., Davis, K., Dietze, M., Dragoni, D.,
1095 Gough, C.M., Grant, R., Hollinger, D., Hufkens, K., Poulter, B.,
1096 McCaughey, H., Raczka, B., Ryu, Y., Schaefer, K., Tian, H., Verbeeck,
1097 H., Zhao, M., Richardson, A.D., 2012. Terrestrial biosphere model
1098 performance for inter-annual variability of land-atmosphere CO₂
1099 exchange. *Glob. Change Biol.* 18, 1971–1987.
1100 <https://doi.org/10.1111/j.1365-2486.2012.02678.x>

1101 Keenan, T.F., Darby, B., Felts, E., Sonnentag, O., Friedl, M.A., Hufkens, K.,
1102 O’Keefe, J., Klosterman, S., Munger, J.W., Toomey, M., Richardson, A.D.,
1103 2014. Tracking forest phenology and seasonal physiology using digital
1104 repeat photography: a critical assessment. *Ecol. Appl.* 24, 1478–1489.

1105 Kennedy, R.E., Yang, Z., Cohen, W.B., 2010. Detecting trends in forest
1106 disturbance and recovery using yearly Landsat time series: 1.
1107 LandTrendr - Temporal segmentation algorithms. *Remote Sens.*
1108 *Environ.* 114, 2897–2910. <https://doi.org/10.1016/j.rse.2010.07.008>

1109 Klemas, V., 2013. Using Remote Sensing to Select and Monitor Wetland
1110 Restoration Sites: An Overview. *J. Coast. Res.* 29, 958–970.

1111 Klosterman, S.T., Hufkens, K., Gray, J.M., Melaas, E., Sonnentag, O., Lavine,
1112 I., Mitchell, L., Norman, R., Friedl, M.A., Richardson, A.D., 2014.
1113 Evaluating remote sensing of deciduous forest phenology at multiple
1114 spatial scales using PhenoCam imagery. *Biogeosciences* 11, 4305–
1115 4320. <https://doi.org/10.5194/bg-11-4305-2014>

1116 Knox, S.H., Dronova, I., Sturtevant, C., Oikawa, P.Y., Matthes, J.H., Verfaillie,
1117 J., Baldocchi, D., 2017. Using digital camera and Landsat imagery with
1118 eddy covariance data to model gross primary production in restored
1119 wetlands. *Agric. For. Meteorol.* 237, 233–245.
1120 <https://doi.org/10.1016/j.agrformet.2017.02.020>

1121 Knox, S.H., Sturtevant, C., Matthes, J.H., Koteen, L., Verfaillie, J., Baldocchi,
1122 D., 2015. Agricultural peatland restoration: effects of land-use change
1123 on greenhouse gas (CO₂ and CH₄) fluxes in the Sacramento-San
1124 Joaquin Delta. *Glob. Change Biol.* 21, 750–765. [https://doi.org/10.1111/](https://doi.org/10.1111/gcb.12745)
1125 [gcb.12745](https://doi.org/10.1111/gcb.12745)

1126 Kotchenova, S.Y., Vermote, E.F., 2007. Validation of a vector version of the
1127 6S radiative transfer code for atmospheric correction of satellite data
1128 Part II Homogeneous Lambertian and anisotropic surfaces. *Appl. Opt.*
1129 46, 4455. <https://doi.org/10.1364/AO.46.004455>

1130 Kruskal, W.H., Wallis, W.A., 1952. Use of Ranks in One-Criterion Variance
1131 Analysis. *Journal of the American Statistical Association* 47, 583–621.
1132 <https://doi.org/10.1080/01621459.1952.10483441>

1133 Larsen, L.G., Harvey, J.W., 2011. Modeling of hydroecological feedbacks
1134 predicts distinct classes of landscape pattern, process, and restoration
1135 potential in shallow aquatic ecosystems. *Geomorphology* 126, 279–
1136 296. <https://doi.org/10.1016/j.geomorph.2010.03.015>

1137 LaRue, E.A., Atkins, J.W., Dahlin, K., Fahey, R., Fei, S., Gough, C., Hardiman,
1138 B.S., 2018. Linking Landsat to terrestrial LiDAR: Vegetation metrics of
1139 forest greenness are correlated with canopy structural complexity. *Int.*
1140 *J. Appl. Earth Obs. Geoinformation* 73, 420–427.
1141 <https://doi.org/10.1016/j.jag.2018.07.001>

1142 Lenssen, J.P.M., Menting, F.B.J., van der Putten, W.H., Blom, C.W.P.M., 1999.
1143 Effects of sediment type and water level on biomass production of
1144 wetland plant species. *Aquat. Bot.* 64, 151–165.
1145 [https://doi.org/10.1016/S0304-3770\(99\)00012-1](https://doi.org/10.1016/S0304-3770(99)00012-1)

1146 Ma, S., Osuna, J.L., Verfaillie, J., Baldocchi, D.D., 2017. Photosynthetic
1147 responses to temperature across leaf-canopy-ecosystem scales: a 15-
1148 year study in a Californian oak-grass savanna. *Photosynth. Res.* 132,
1149 277–291. <https://doi.org/10.1007/s11120-017-0388-5>

1150 Machado-Machado, E.A., Neeti, N., Eastman, J.R., Chen, H., 2011.
1151 Implications of space-time orientation for Principal Components
1152 Analysis of Earth observation image time series. *Earth Sci. Inform.* 4,
1153 117–124. <https://doi.org/10.1007/s12145-011-0082-7>

1154 Matthes, J.H., Sturtevant, C., Verfaillie, J., Knox, S., Baldocchi, D., 2014.
1155 Parsing the variability in CH₄ flux at a spatially heterogeneous
1156 wetland: Integrating multiple eddy covariance towers with high-
1157 resolution flux footprint analysis. *J. Geophys. Res.-Biogeosciences* 119,
1158 1322–1339. <https://doi.org/10.1002/2014JG002642>

1159 Matthews, J.W., Spyreas, G., Endress, A.G., 2009. Trajectories of vegetation-
1160 based indicators used to assess wetland restoration progress. *Ecol.*
1161 *Appl.* 19, 2093–2107. <https://doi.org/10.1890/08-1371.1>

1162 McNicol, G., Sturtevant, C.S., Knox, S.H., Dronova, I., Baldocchi, D.D., Silver,
1163 W.L., 2017. Effects of seasonality, transport pathway, and spatial
1164 structure on greenhouse gas fluxes in a restored wetland. *Glob.*
1165 *Change Biol.* 23, 2768–2782. <https://doi.org/10.1111/gcb.13580>

1166 Melaas, E.K., Friedl, M.A., Richardson, A.D., 2016. Multiscale modeling of
1167 spring phenology across Deciduous Forests in the Eastern United
1168 States. *Glob. Change Biol.* 22, 792–805.
1169 <https://doi.org/10.1111/gcb.13122>

1170 Melaas, E.K., Friedl, M.A., Zhu, Z., 2013. Detecting interannual variation in
1171 deciduous broadleaf forest phenology using Landsat TM/ETM plus data.
1172 *Remote Sens. Environ.* 132, 176–185.
1173 <https://doi.org/10.1016/j.rse.2013.01.011>

1174 Melaas, E.K., Sulla-Menashe, D., Friedl, M.A., 2018. Multidecadal Changes
1175 and Interannual Variation in Springtime Phenology of North American
1176 Temperate and Boreal Deciduous Forests. *Geophys. Res. Lett.* 45,
1177 2679–2687. <https://doi.org/10.1002/2017GL076933>

1178 Miller, R.L., Fujii, R., 2010. Plant community, primary productivity, and
1179 environmental conditions following wetland re-establishment in the
1180 Sacramento-San Joaquin Delta, California. *Wetl. Ecol. Manag.* 18, 1-16.
1181 <https://doi.org/10.1007/s11273-009-9143-9>

1182 Minke, M., Augustin, J., Burlo, A., Yarmashuk, T., Chuvashova, H., Thiele, A.,
1183 Freibauer, A., Tikhonov, V., Hoffmann, M., 2016. Water level,
1184 vegetation composition, and plant productivity explaining greenhouse gas
1185 fluxes in temperate cutover fens after inundation. *Biogeosciences* 13,
1186 3945-3970. <https://doi.org/10.5194/bg-13-3945-2016>

1187 Misra, G., Buras, A., Menzel, A., 2016. Effects of Different Methods on the
1188 Comparison between Land Surface and Ground Phenology—A
1189 Methodological Case Study from South-Western Germany. *Remote*
1190 *Sens.* 8, 753. <https://doi.org/10.3390/rs8090753>

1191 Mitsch, W.J., Bernal, B., Nahlik, A.M., Mander, U., Zhang, L., Anderson, C.J.,
1192 Jorgensen, S.E., Brix, H., 2013. Wetlands, carbon, and climate change.
1193 *Landsc. Ecol.* 28, 583-597. <https://doi.org/10.1007/s10980-012-9758-8>

1194 Mo, Y., Momen, B., Kearney, M.S., 2015. Quantifying moderate resolution
1195 remote sensing phenology of Louisiana coastal marshes. *Ecol. Model.*
1196 312, 191-199. <https://doi.org/10.1016/j.ecolmodel.2015.05.022>

1197 Mood, A.M., 1950. *Introduction to the Theory of Statistics*. New York:
1198 McGraw-Hill.

1199 O'Connell, J.L., Alber, M., Pennings, S.C., 2019. Microspatial Differences in
1200 Soil Temperature Cause Phenology Change on Par with Long-Term
1201 Climate Warming in Salt Marshes. *Ecosystems*. <https://doi.org/10.1007/s10021-019-00418-1>

1202

1203 Oikawa, P.Y., Jenerette, G.D., Knox, S.H., Sturtevant, C., Verfaillie, J.,
1204 Dronova, I., Poindexter, C.M., Eichelmann, E., Baldocchi, D.D., 2017.
1205 Evaluation of a hierarchy of models reveals importance of substrate
1206 limitation for predicting carbon dioxide and methane exchange in
1207 restored wetlands: Model for Wetland Greenhouse Gas Fluxes. *J.*
1208 *Geophys. Res. Biogeosciences* 122, 145-167.
1209 <https://doi.org/10.1002/2016JG003438>

1210 Rejšková, A., Čížková, H., Brom, J., Pokorný, J., 2012. Transpiration,
1211 evapotranspiration and energy fluxes in a temperate wetland
1212 dominated by *Phalaris arundinacea* under hot summer conditions.
1213 *Ecohydrology* 5, 19-27. <https://doi.org/10.1002/eco.184>

1214 Richardson, A.D., Anderson, R.S., Arain, M.A., Barr, A.G., Bohrer, G., Chen, G.,
1215 Chen, J.M., Ciais, P., Davis, K.J., Desai, A.R., Dietze, M.C., Dragoni, D.,
1216 Garrity, S.R., Gough, C.M., Grant, R., Hollinger, D.Y., Margolis, H.A.,
1217 McCaughey, H., Migliavacca, M., Monson, R.K., Munger, J.W., Poulter,
1218 B., Raczka, B.M., Ricciuto, D.M., Sahoo, A.K., Schaefer, K., Tian, H.,
1219 Vargas, R., Verbeeck, H., Xiao, J., Xue, Y., 2012. Terrestrial biosphere
1220 models need better representation of vegetation phenology: results
1221 from the North American Carbon Program Site Synthesis. *Glob. Change*
1222 *Biol.* 18, 566-584. <https://doi.org/10.1111/j.1365-2486.2011.02562.x>

1223 Richardson, A.D., Hufkens, K., Milliman, T., Aubrecht, D.M., Chen, M., Gray,
1224 J.M., Johnston, M.R., Keenan, T.F., Klosterman, S.T., Kosmala, M.,
1225 Melaas, E.K., Friedl, M.A., Froking, S., 2018. Tracking vegetation
1226 phenology across diverse North American biomes using PhenoCam
1227 imagery. *Sci. Data* 5, 180028. <https://doi.org/10.1038/sdata.2018.28>
1228 Rocha, A.V., Goulden, M.L., 2010. Drought legacies influence the long-term
1229 carbon balance of a freshwater marsh. *J. Geophys. Res.* 115, G00H02.
1230 <https://doi.org/10.1029/2009JG001215>
1231 Rocha, A.V., Goulden, M.L., 2009. Why is marsh productivity so high? New
1232 insights from eddy covariance and biomass measurements in a Typha
1233 marsh. *Agric. For. Meteorol.* 149, 159-168.
1234 <https://doi.org/10.1016/j.agrformet.2008.07.010>
1235 Rocha, A.V., Potts, D.L., Goulden, M.L., 2008. Standing litter as a driver of
1236 interannual CO(2) exchange variability in a freshwater marsh. *J.*
1237 *Geophys. Res.-Biogeosciences* 113, G04020.
1238 <https://doi.org/10.1029/2008JG000713>
1239 Ryu, Y., Baldocchi, D.D., Verfaillie, J., Ma, S., Falk, M., Ruiz-Mercado, I., Hehn,
1240 T., Sonnentag, O., 2010. Testing the performance of a novel spectral
1241 reflectance sensor, built with light emitting diodes (LEDs), to monitor
1242 ecosystem metabolism, structure and function. *Agric. For. Meteorol.*
1243 150, 1597-1606. <https://doi.org/10.1016/j.agrformet.2010.08.009>
1244 Schaffer-Smith, D., Swenson, J.J., Reiter, M.E., Isola, J.E., 2018. Quantifying
1245 shorebird habitat in managed wetlands by modeling shallow water
1246 depth dynamics. *Ecol. Appl.* 28, 1534-1545.
1247 <https://doi.org/10.1002/eap.1732>
1248 Schile, L.M., Byrd, K.B., Windham-Myers, L., Kelly, M., 2013. Accounting for
1249 non-photosynthetic vegetation in remote-sensing-based estimates of
1250 carbon flux in wetlands. *Remote Sens. Lett.* 4, 542-551. <https://doi.org/10.1080/2150704X.2013.766372>
1251 Sharma, P., Jones, C.E., Dudas, J., Bawden, G.W., Deverel, S., 2016.
1252 Monitoring of subsidence with UAVSAR on Sherman Island in
1253 California's Sacramento-San Joaquin Delta. *Remote Sens. Environ.* 181,
1254 218-236. <https://doi.org/10.1016/j.rse.2016.04.012>
1255 Smesrud, J.K., Boyd, M.S., Cuenca, R.H., Eisner, S.L., 2014. A mechanistic
1256 energy balance model for predicting water temperature in surface flow
1257 wetlands. *Ecol. Eng.* 67, 11-24.
1258 <https://doi.org/10.1016/j.ecoleng.2014.03.006>
1259 Smith, M.L., Ollinger, S.V., Martin, M.E., Aber, J.D., Hallett, R.A., Goodale, C.L.,
1260 2002. Direct estimation of aboveground forest productivity through
1261 hyperspectral remote sensing of canopy nitrogen. *Ecol. Appl.* 12, 1286-
1262 1302.
1263
1264 Sonnentag, O., Detto, M., Vargas, R., Ryu, Y., Runkle, B.R.K., Kelly, M.,
1265 Baldocchi, D.D., 2011. Tracking the structural and functional
1266 development of a perennial pepperweed (*Lepidium latifolium* L.)
1267 infestation using a multi-year archive of webcam imagery and eddy

1268 covariance measurements. *Agric. For. Meteorol.* 151, 916–926. <https://doi.org/10.1016/j.agrformet.2011.02.011>

1269

1270 Sonnentag, O., Hufkens, K., Teshera-Sterne, C., Young, A.M., Friedl, M.,
1271 Braswell, B.H., Milliman, T., O’Keefe, J., Richardson, A.D., 2012. Digital
1272 repeat photography for phenological research in forest ecosystems.
1273 *Agric. For. Meteorol.* 152, 159–177.
1274 <https://doi.org/10.1016/j.agrformet.2011.09.009>

1275 Stefanik, K.C., Mitsch, W.J., 2012. Structural and functional vegetation
1276 development in created and restored wetland mitigation banks of
1277 different ages. *Ecol. Eng.* 39, 104–112.
1278 <https://doi.org/10.1016/j.ecoleng.2011.11.016>

1279 Strachan, I.B., Nugent, K.A., Crombie, S., Bonneville, M.-C., 2015. Carbon
1280 dioxide and methane exchange at a cool-temperate freshwater marsh.
1281 *Environ. Res. Lett.* 10, 065006. [https://doi.org/10.1088/1748-](https://doi.org/10.1088/1748-9326/10/6/065006)
1282 [9326/10/6/065006](https://doi.org/10.1088/1748-9326/10/6/065006)

1283 Suding, K.N., 2011. Toward an Era of Restoration in Ecology: Successes,
1284 Failures, and Opportunities Ahead, in: Futuyma, D.J., Shaffer, H.B.,
1285 Simberloff, D. (Eds.), *Annual Review of Ecology, Evolution, and*
1286 *Systematics*, Vol 42. pp. 465–487.

1287 Sulla-Menashe, D., Kennedy, R.E., Yang, Z., Braaten, J., Krankina, O.N., Friedl,
1288 M.A., 2014. Detecting forest disturbance in the Pacific Northwest from
1289 MODIS time series using temporal segmentation. *Remote Sens.*
1290 *Environ.* 151, 114–123. <https://doi.org/10.1016/j.rse.2013.07.042>

1291 Taddeo, S., Dronova, I., 2019. Geospatial Tools for the Large-Scale
1292 Monitoring of Wetlands in the San Francisco Estuary: Opportunities and
1293 Challenges. *San Franc. Estuary Watershed Sci.* 17.
1294 <https://doi.org/10.15447/sfew.2019v17iss2art2>

1295 Taddeo, S., Dronova, I., 2018. Indicators of vegetation development in
1296 restored wetlands. *Ecol. Indic.* 94, 454–467.
1297 <https://doi.org/10.1016/j.ecolind.2018.07.010>

1298 Tan, B., Morissette, J.T., Wolfe, R.E., Gao, F., Ederer, G.A., Nightingale, J.,
1299 Pedelty, J.A., 2011. An Enhanced TIMESAT Algorithm for Estimating
1300 Vegetation Phenology Metrics From MODIS Data. *IEEE J. Sel. Top. Appl.*
1301 *Earth Obs. Remote Sens.* 4, 361–371.
1302 <https://doi.org/10.1109/JSTARS.2010.2075916>

1303 Toomey, M., Friedl, M.A., Froking, S., Hufkens, K., Klosterman, S., Sonnentag,
1304 O., Baldocchi, D.D., Bernacchi, C.J., Biraud, S.C., Bohrer, G., Brzostek,
1305 E., Burns, S.P., Coursolle, C., Hollinger, D.Y., Margolis, H.A.,
1306 McCaughey, H., Monson, R.K., Munger, J.W., Pallardy, S., Phillips, R.P.,
1307 Torn, M.S., Wharton, S., Zeri, M., Richardson, A.D., 2015. Greenness
1308 indices from digital cameras predict the timing and seasonal dynamics
1309 of canopy-scale photosynthesis. *Ecol. Appl.* 25, 99–115. <https://doi.org/10.1890/14-0005.1>

1310

1311 Tóth, V.R., 2018. Monitoring Spatial Variability and Temporal Dynamics of
1312 Phragmites Using Unmanned Aerial Vehicles. *Frontiers in Plant Science*
1313 9. <https://doi.org/10.3389/fpls.2018.00728>

1314 Villa, J.A., Bernal, B., 2018. Carbon sequestration in wetlands, from science to
1315 practice: An overview of the biogeochemical process, measurement
1316 methods, and policy framework. *Ecol. Eng.* 114, 115-128.
1317 <https://doi.org/10.1016/j.ecoleng.2017.06.037>

1318 Vogelmann, J.E., Gallant, A.L., Shi, H., Zhu, Z., 2016. Perspectives on
1319 monitoring gradual change across the continuity of Landsat sensors
1320 using time-series data. *Remote Sens. Environ.* 185, 258-270.
1321 <https://doi.org/10.1016/j.rse.2016.02.06>

1322 Vrieling, A., Meroni, M., Darvishzadeh, R., Skidmore, A.K., Wang, T., Zurita-
1323 Milla, R., Oosterbeek, K., O'Connor, B., Paganini, M., 2018. Vegetation
1324 phenology from Sentinel-2 and field cameras for a Dutch barrier island.
1325 *Remote Sensing of Environment* 215, 517-529. <https://doi.org/10.1016/j.rse.2018.03.014>

1327 Woebbecke, D., Meyer, G., Vonbargen, K., Mortensen, D., 1995. Color
1328 indexes for weed identification under various soil, residue, and lighting
1329 conditions. *Trans. Asae* 38, 259-269.

1330 Wolf, S., Keenan, T.F., Fisher, J.B., Baldocchi, D.D., Desai, A.R., Richardson,
1331 A.D., Scott, R.L., Law, B.E., Litvak, M.E., Brunsell, N.A., Peters, W., van
1332 der Laan-Luijkx, I.T., 2016. Warm spring reduced carbon cycle impact
1333 of the 2012 US summer drought. *Proc. Natl. Acad. Sci.* 113, 5880-5885.
1334 <https://doi.org/10.1073/pnas.1519620113>

1335 Woodcock, C.E., Loveland, T.R., Herold, M., Bauer, M.E., 2020. Transitioning
1336 from change detection to monitoring with remote sensing: A paradigm
1337 shift. *Remote Sens. Environ.* 238, 111558.
1338 <https://doi.org/10.1016/j.rse.2019.111558>

1339 Zhang, G., Xiao, X., Dong, J., Kou, W., Jin, C., Qin, Y., Zhou, Y., Wang, J.,
1340 Menarguez, M.A., Biradar, C., 2015. Mapping paddy rice planting areas
1341 through time series analysis of MODIS land surface temperature and
1342 vegetation index data. *ISPRS J. Photogramm. Remote Sens.* 106, 157-
1343 171. <https://doi.org/10.1016/j.isprsjprs.2015.05.011>

1344 Zhang, L., Wang, B., 2016. Intraspecific interactions shift from competitive to
1345 facilitative across a low to high disturbance gradient in a salt marsh.
1346 *Plant Ecol.* 217, 959-967. <https://doi.org/10.1007/s11258-016-0621-x>

1347 Zhang, L., Weng, Q., 2016. Annual dynamics of impervious surface in the
1348 Pearl River Delta, China, from 1988 to 2013, using time series Landsat
1349 imagery. *ISPRS J. Photogramm. Remote Sens.* 113, 86-96.
1350 <https://doi.org/10.1016/j.isprsjprs.2016.01.003>

1351 Zhao, Q., Bai, J., Huang, L., Gu, B., Lu, Q., Gao, Z., 2016. A review of
1352 methodologies and success indicators for coastal wetland restoration.
1353 *Ecol. Indic.* 60, 442-452. <https://doi.org/10.1016/j.ecolind.2015.07.003>

1354 Zhu, Z., 2017. Change detection using landsat time series: A review of
1355 frequencies, preprocessing, algorithms, and applications. *ISPRS J.*
1356 *Photogramm. Remote Sens.* 130, 370-384.
1357 <https://doi.org/10.1016/j.isprsjprs.2017.06.013>

1358

1359 **List of Figures**

1360 **Figure 1.** Study area in the Sacramento-San Joaquin Delta, California, USA.

1361 Background image: aerial photo from the National Agriculture Imagery

1362 Program (NAIP) for California.

1363 **Figure 2.** Statistical distributions of the main phenological metrics

1364 estimated from Landsat (darker fill), RapidEye at the original 5m spatial

1365 resolution (moderately dark fill) and RapidEye aggregated to 30m spatial

1366 resolution (lightest fill) image inputs within biometeorological footprints of

1367 East End (EE), Mayberry Farms (MB) and West Pond (WP) wetland sites: a)

1368 start of greening (SOG), b) end of greening (EOG), c) start of senescence

1369 (SOS), d) end of senescence (EOS), e) duration of the season (DUR) and f)

1370 maximum greenness (MAXG).

1371 **Figure 3.** Spatial distributions of phenological metrics computed from 5m

1372 RapidEye Enhanced Vegetation Index (EVI) within biometeorological flux

1373 footprints of three wetland sites: a-c) start of greening (SOG), d-f) end of

1374 greening (EOG), g-i) start of senescence (SOS), j-l) end of senescence (EOS),

1375 m-o) duration of the growing season (DUR), and p-r) reference high-

1376 resolution aerial imagery. Vertical arrangements represent the 19-year old

1377 West Pond (WP) wetland (a,d,g,j,m,p), the 6-year old Mayberry Farms (MB)

1378 wetland (b,e,h,k,n,q) and the 2-year old East End (EE) wetland (c,f,i,l,o,r).

1379 **Figure 4.** Spatial distributions of phenological curve fitting error (left panels)

1380 from models fitted to 30m Landsat and 5m RapidEye input series and

1381 maximum greenness (right panels) at three wetland sites: a-b) West Pond,
1382 RapidEye; c-d) West Pond, Landsat; e-f) Mayberry Farms, RapidEye; g-h)
1383 Mayberry Farms, Landsat; i-j) East End, RapidEye, and k-l) East End, Landsat.

1384 **Figure 5.** Seasonal trajectories of field-measured a) eddy covariance net
1385 ecosystem exchange (NEE, $\text{gC-CO}_2\text{m}^{-2}\text{d}^{-1}$; negative sign indicates net
1386 ecosystem uptake), b) phenocam green chromatic coordinate (GCC) spectral
1387 index, and c) water temperature measured at 10cm for Mayberry Farms (MB)
1388 and East End (EE) sites and at 8cm for West Pond (WP). All variables are
1389 plotted as 5-day moving window averages.

1390 **Figure 6.** The agreement between site-median satellite-based days of year
1391 (DOYs) representing start and end transitions of the Enhanced Vegetation
1392 Index (EVI) trajectories from 30m Landsat imagery and 5m RapidEye
1393 imagery and the corresponding transitions in the trajectories of phenocam-
1394 based green chromatic coordinate (GCC) spectral index (a) and net
1395 ecosystem exchange (NEE) for CO_2 measured by eddy covariance stations
1396 (b). Equations represent the fitted linear regression models where y denotes
1397 site median transition dates estimated from satellite-based EVI series, and x
1398 denotes the transition dates from the time series of a respective field-
1399 measured metric.

1400 **Figure 7.** The associations between satellite EVI and average daily water
1401 temperature on the corresponding image dates for a) Landsat at 30m spatial
1402 resolution, and b) RapidEye at 5m spatial resolution. Equations represent the

1403 fitted linear regression models where y denotes EVI and x denotes water

1404 temperature of a given site.

1405

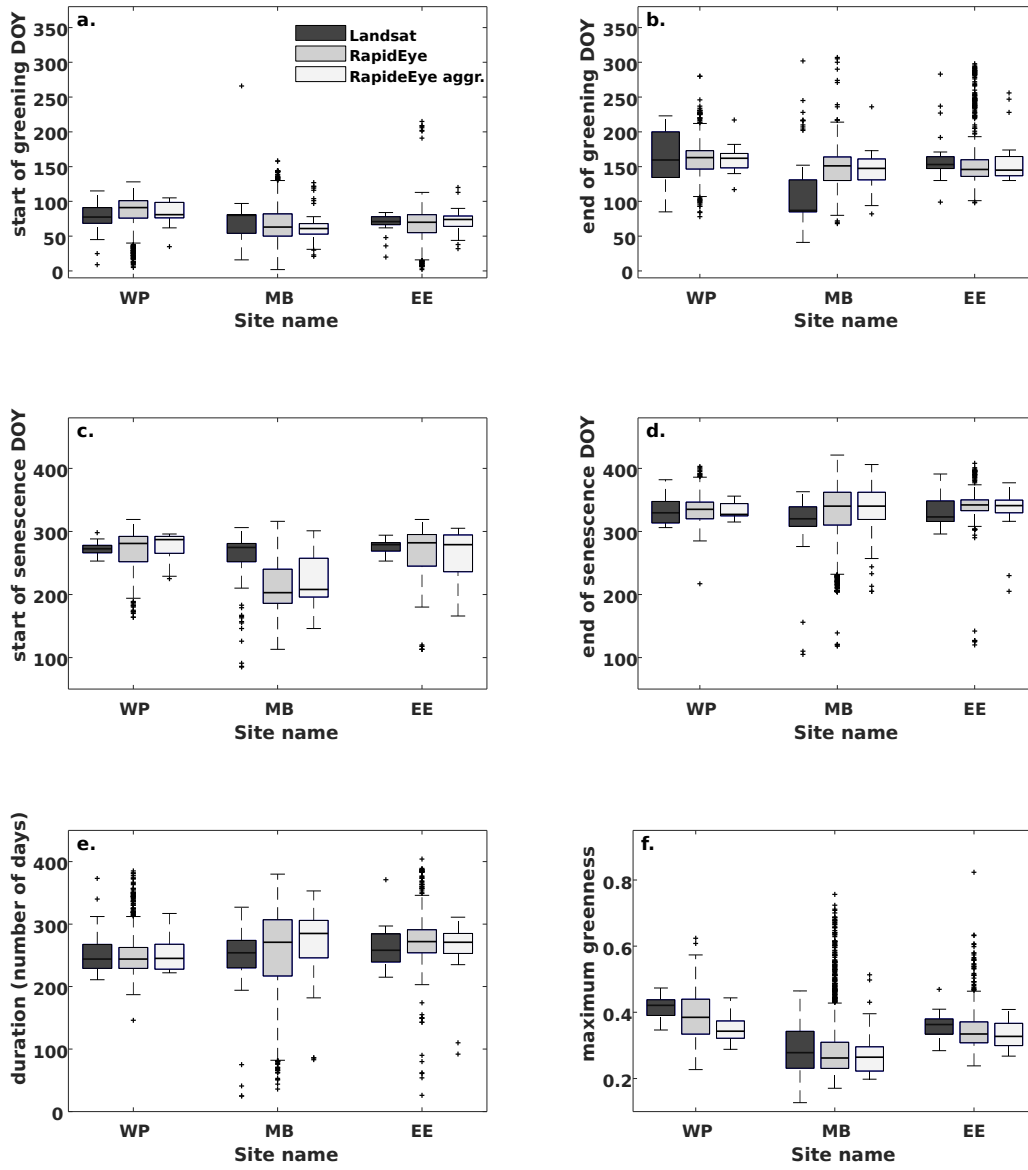
1406 **Figures**

1407

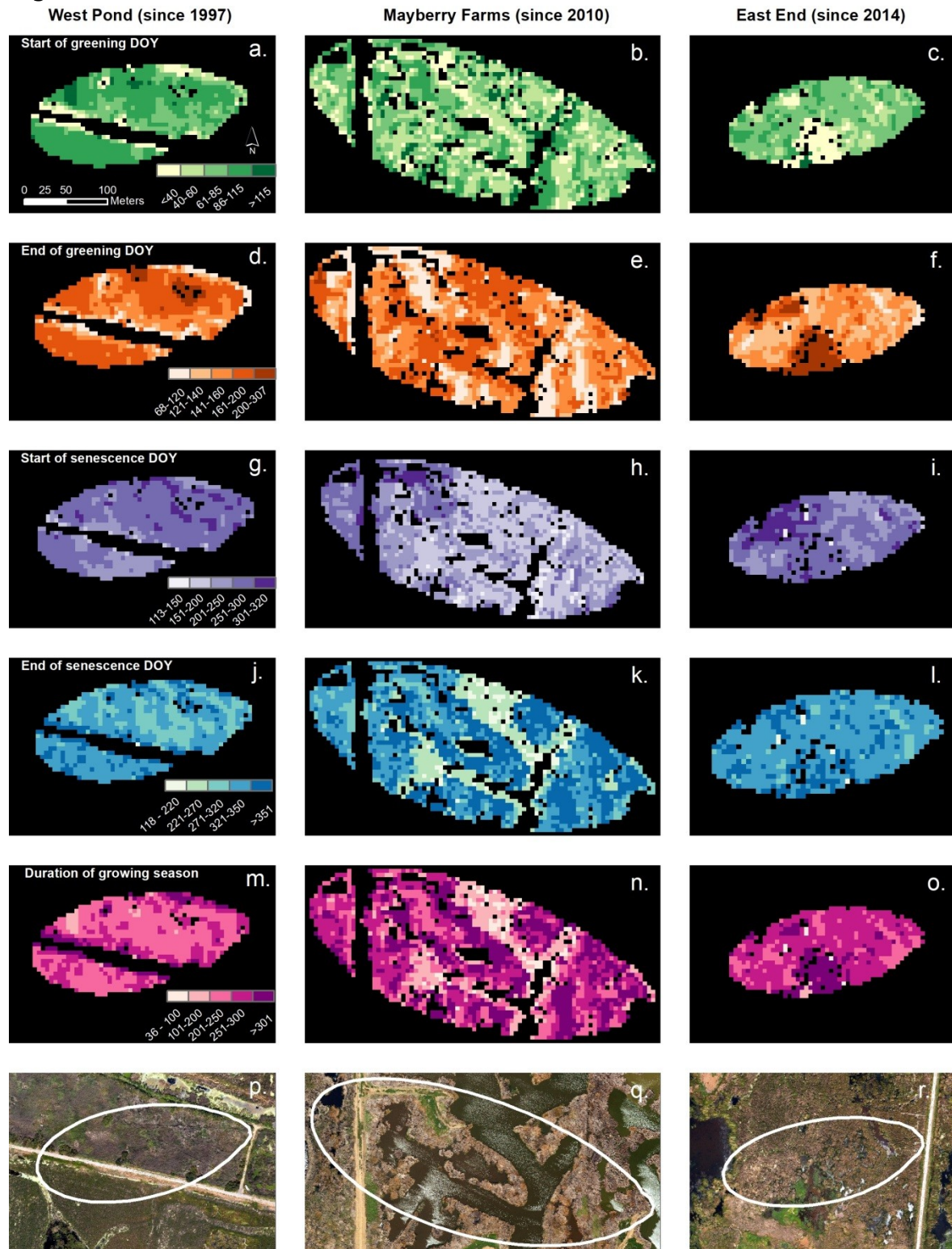
1408 Figure 1



1409

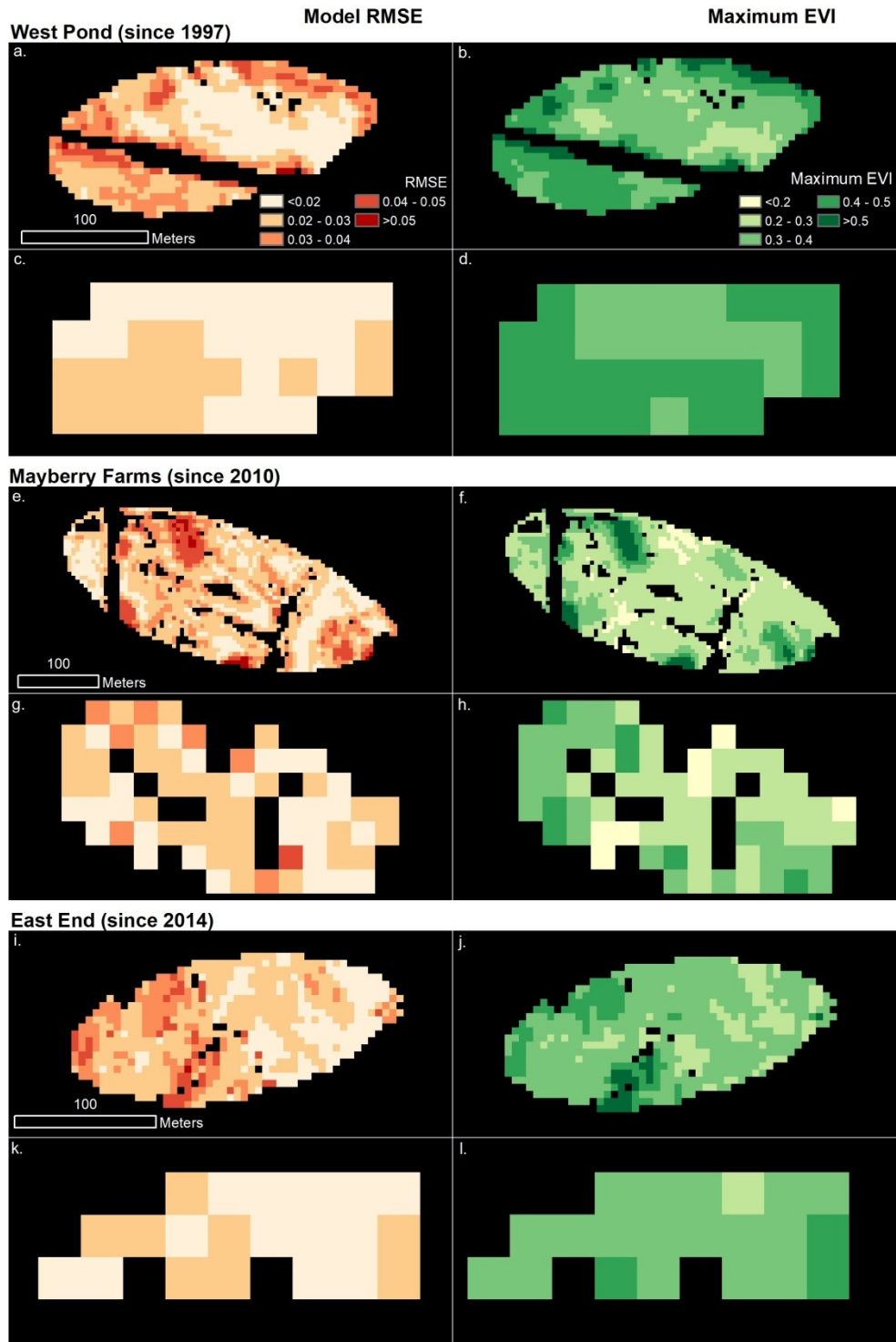


1412 Figure 3



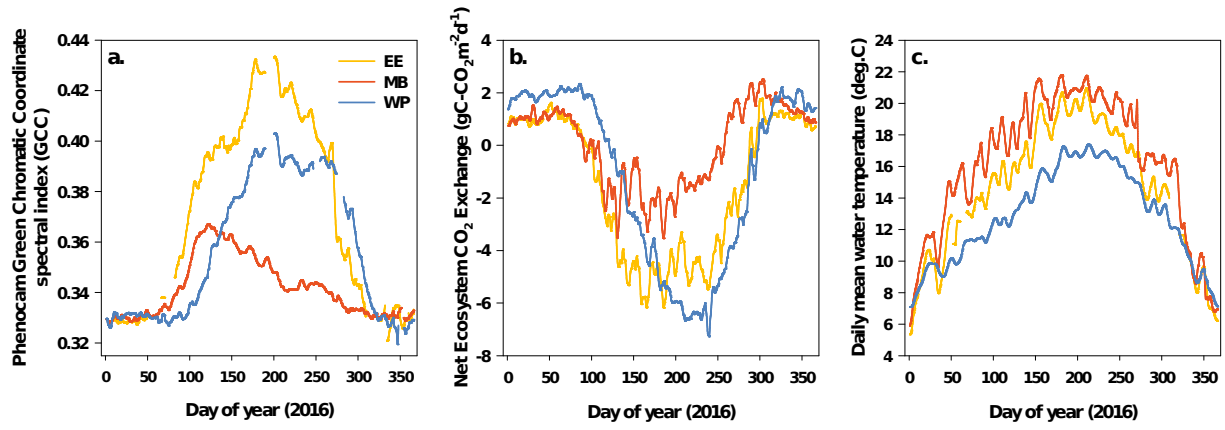
1413
1414

1415 Figure 4



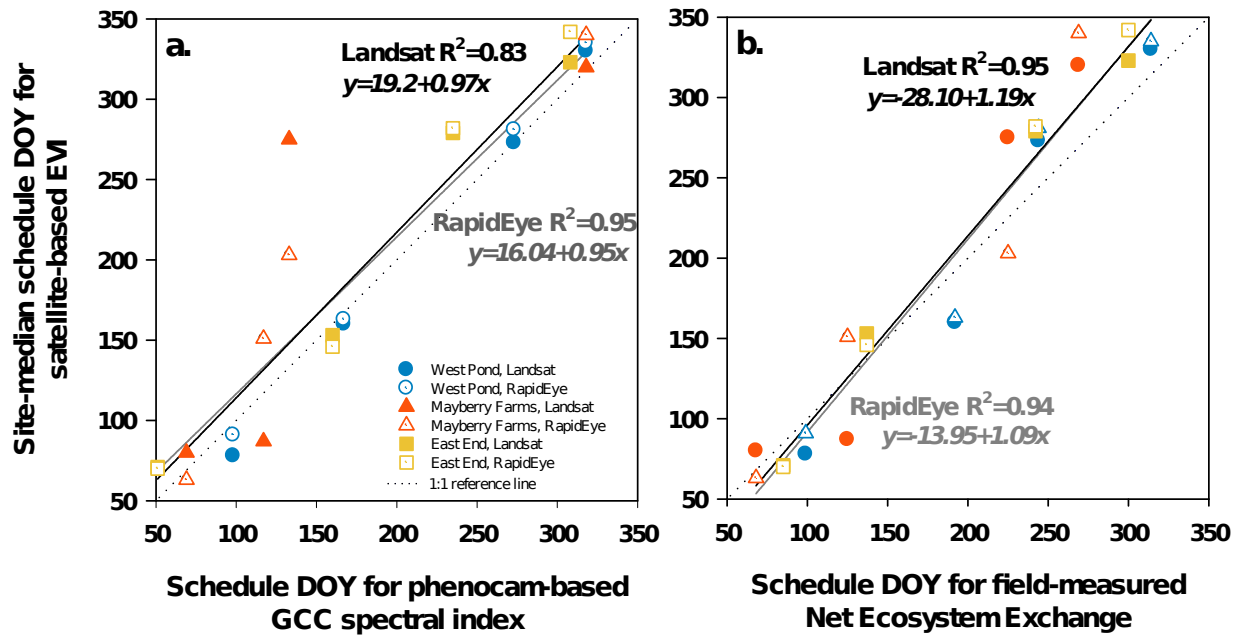
1416
1417

1418 Figure 5
1419



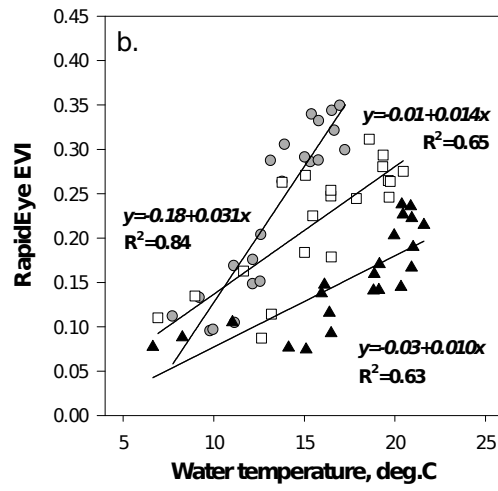
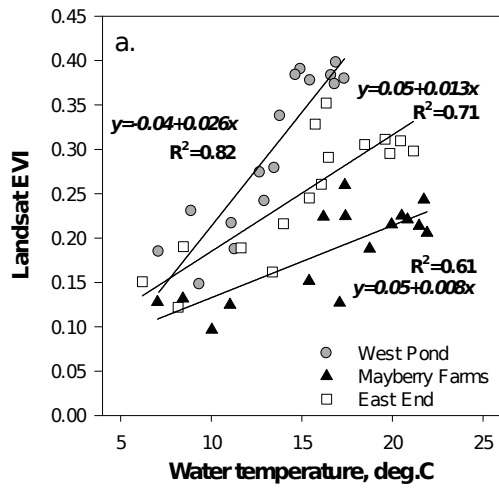
1420
1421

1422 Figure 6



1423
1424

1425 Figure 7



1426
1427

1428 **Tables**

1429 **Table 1.** Landscape metrics of vegetation distribution and field

1430 measurements of canopy structure, by wetland site. All metrics except patch

1431 density and percentage values show means of the plot or site measurements

1432 with standard deviation in parentheses.

Metric type	Metric	Site		
		West Pond (WP), est. 1997	Mayberry Farms (MB), est. 2010	East End (EE), est. 2014
Spatial extent	Whole wetland area, km ²	0.032	1.242	2.995
	Flux footprint area (90 th percentile), km ²	0.022	0.054	0.018
Landscape metrics based on aerial images*	Percent vegetated cover (whole site)	99.7%	64.4%	82.2%
	Percent vegetated (flux tower footprint; 90 th percentile)	74.0%	55.7%	83.2%
	Patch density (number of patches/100 ha)	19.29	81.56	42.70
	Mean Patch Area of vegetated patches, km ²	0.05 (0)	0.01 (0.09)	0.02 (0.28)
	Mean Shape Index of vegetated patches	1.42 (0)	1.58 (1.55)	1.48 (1.50)
Field measurements (summer 2016) ‡	Green one-sided leaf area index, m ² m ⁻²	3.1 (1.7)	1.9 (2.3)	3.8 (2.2)
	Canopy height, cm	335.5 (29.1)	223.7 (27.6)	282.4 (29.1)
	Litter height, cm	211.4 (39.4)	211.6 (41.5)	161.8 (16.4)
	Litter volume (m ³ per 0.09m ² plot)	0.134 (0.05)	0.100 (0.04)	0.022 (0.02)
	Percent dead vegetation in plot cover	58.9%	51.7%	54.2%
	Water depth, cm	19.6 (11.3)	37.9 (14.8)	66.3 (17.6)

1433 * Landscape metrics are based on vegetation patches delineated from 1-m spatial resolution
1434 aerial imagery publicly available from USDA's National Agriculture Inventory Program (NAIP)
1435 for the summer 2016.

1436 ‡Field sampling was conducted between August 2 and 8, 2016 within 0.3m×0.3m sampling
1437 plots (24 plots in West Pond, 36 plots in Mayberry Farms, and 20 plots in East End). Litter
1438 height corresponds to the height of standing litter, approximated to the nearest 0.05m.

1439 Litter volume is based on visually estimated percent litter cover class (0-25%, 25-50%, 50-
1440 75%, >75%) summed across the 0.2-m increments along the vertical dimension of the
1441 canopy above each 0.3m×0.3m plot. Percent dead vegetation is a visual estimation of the
1442 percentage of the sampling plot covered by dead vegetation versus green plants or other
1443 surfaces (open water, bare soil).

1444 **Table 2.** Key phenological metrics and ecosystem variables used in this
 1445 study.

Abbreviation	Explanation	Definition
<i>Wetland site names</i>		
WP	West Pond	The oldest study site (restored in 1997)
MB	Mayberry Farms	The intermediate-aged site (restored in 2010)
EE	East End	The youngest study site (restored in 2014)
<i>Spectral vegetation indices</i>		
EVI	Enhanced Vegetation Index	Huete et al. 2002
GCC	Green Chromatic Coordinate Index	Woebbecke et al. 1995
<i>Phenological metrics</i>		
DOY	Day of year	Consecutive day of year starting from Jan 1, 2016. In cases where growing season and its mathematical analysis extended beyond December 31, 2016, DOY values exceeded 365 according to the additional dates.
SOG	Start of greening	DOY representing the first major curvature point in the phenological curve indicating the onset of spring increase.
EOG	End of greening	DOY representing the second major curvature point in the phenological curve indicating the slowdown in spring EVI increase approaching maximum greenness.
SOS	Start of senescence	DOY representing the third major curvature point in the phenological curve indicating the onset of EVI decline (senescence).
EOS	End of senescence	DOY representing the last major curvature point in the phenological curve indicating the end of the fall spectral index decline.
DUR	Duration of the growing season	The difference between DOYs corresponding to EOS and SOG.
MAXG	Maximum greenness	Maximum value of the seasonal EVI.
RMSE	Root mean square error	Standard deviation of residuals in the phenological curve model

		indicating the deviation of satellite-measured greenness values from the modeled trajectory.
<hr/>		
<i>Ecosystem variables</i>		
NEE	Net ecosystem exchange (for CO ₂)	Net exchange of CO ₂ carbon between the wetland ecosystem and the atmosphere based on eddy covariance CO ₂ flux data.
LAI	Leaf area index	One-sided green canopy leaf area per unit ground area.
<hr/>		

1447 **Table 3.** Slope and intercept comparisons between regressions with DOYs
 1448 for phenological transition dates derived from satellite inputs or seasonal
 1449 trajectories of field-measured Green Chromatic Coordinate greenness (GCC)
 1450 and net ecosystem exchange for CO₂ (NEE).

1451

Response variable	Predictor variable 1	Compared to model	P-value, slope comparison	P-value, intercept comparison
Transition DOY for GCC	Site-median DOYs of key stages (Landsat)	Slope=1, intercept=0	0.226	0.549
Transition DOY for GCC	Site-median DOYs of key stages (RapidEye)	Slope=1, intercept=0	0.186	0.926
Transition DOY for NEE	Site-median DOYs of key stages (Landsat)	Slope=1, intercept=0	0.004	0.031
Transition DOY for NEE	Site-median DOYs of key stages (RapidEye)	Slope=1, intercept=0	0.005	0.053
Transition DOY for NEE	Site-median DOYs of key stages (Landsat)	With site-median DOYs of key stages from RapidEye	0.983	0.883
Transition DOY for GCC	Site-median DOYs of key stages (Landsat)	With site-median DOYs of key stages from RapidEye	0.663	0.635

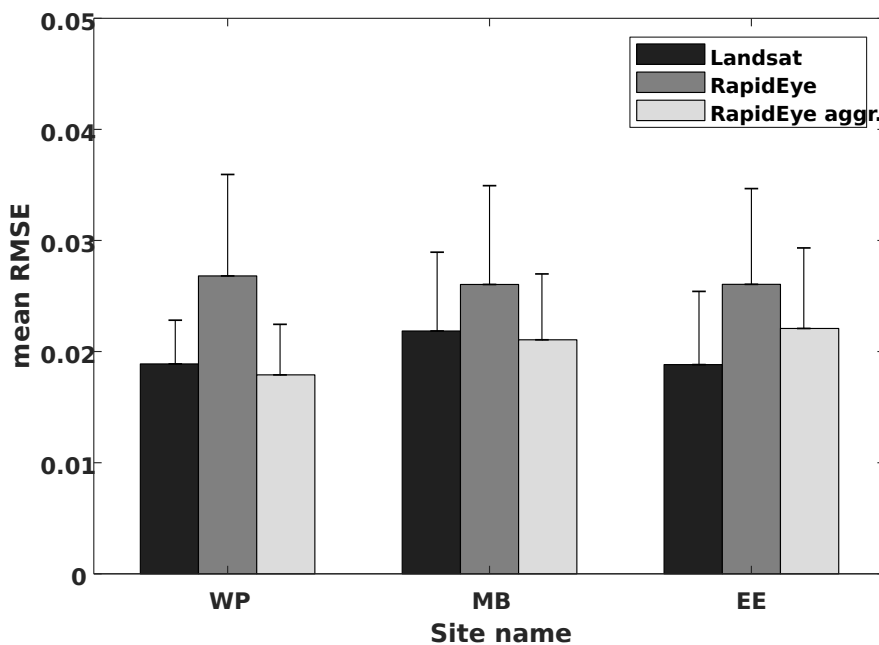
1452

1453

1454 **Appendix**

1455

1456 Figure A1. Root mean square error (RMSE) of per-pixel phenological model
 1457 fitting for three different satellite data inputs (Landsat at 30m spatial
 1458 resolution, RapidEye at the original 5m spatial resolution and RapidEye
 1459 aggregated to 30m spatial resolution) averaged for the CO₂ flux footprints of
 1460 wetland sites West Pond (WP), Mayberry (MB) and East End (EE). Upper error
 1461 bars show standard deviations of RMSE for each respective group.



1462

1463 Table A1. Satellite products and dates used in phenological metric estimation
 1464 (DOY stands for consecutive day of year starting from January 1, 2016).

1465

Month	Year	Date: Landsat-8 Surface Reflectance Tier 1 (DOY)	Date: RapidEye Geocorrected At-sensor Radiance (DOY)
February	2016	4 (35)	15 (46) 22(53)
March	2016	23 (83)	17 (77)

April	201 6	24 (115)	17 (108) 20 (111)
May	201 6	10 (131) 26 (147)	1 (122) 26 (147)
June	201 6	11 (163) 27 (179)	1 (153) 20 (172) 22 (174)
July	201 6	13 (195) 29 (211)	16 (198) 23 (205)
August	201 6	14 (227)	2 (215)
September	201 6	23 (267)	7 (251) 24 (268)
October	201 6	1 (275)	18 (292) 20 (294)
November	201 6	2 (307) 18 (323)	8 (313) 18 (323)
December	201 6	4 (339)	3 (338) 26 (361)
January	201 7	5 (371 since Jan 1, 2016)	

1466

1467 Table A2. Mood's test results for pairwise comparisons of phenological
 1468 metrics between site and sensor pairs. Values represent test chi-square
 1469 statistic estimated using Matlab mediantest function by Keine (2020).

<i>Site pair comparisons for a given satellite input</i>									
Metri c	Landsat (30m)			RapidEye (5m)			Aggregated RapidEye (30m)		
	WP&MB	WP&EE	MB&EE	WP&MB	WP&EE	MB&EE	WP&MB	WP&EE	MB&EE
SOG	1.71	2.67	13.12*	438.15*	281.69*	37.82*	15.08*	3.94*	11.03*
EOG	24.38*	2.67	23.63*	112.72*	167.99*	23.39*	2.06	2.95	0.23
SOS	1.02	2.30	1.16	856.81*	0.23	738.61*	22.39*	1.17	14.93*
EOS	2.57	0.03	0.20	12.26*	37.97*	4.26*	1.72	1.43	0.23
DUR	1.34	2.30	0.10	145.18*	249.35*	0.57	5.82*	4.36*	4.03*
MAXG	50.00*	17.53*	18.52*	882.24*	169.47*	695.58*	21.74*	1.17	23.89*

<i>Satellite input comparisons for a given site</i>			
Metri c	Landsat (30m) & original RapidEye data (5m)		Original (5m) & aggregated (30m) RapidEye data
	Landsat & aggregated RapidEye data (30m)		

	WP	MB	EE	WP	MB	EE	WP	MB	EE
SOG	7.85*	13.32*	0.09	2.58	23.94*	1.97	0.37	4.57*	2.88
EOG	0.39	23.59*	6.13*	0.16	29.48*	3.67	0.04	0.39	0.08
SOS	15.62*	25.42*	5.44*	2.58	29.52*	0.73	0.73	2.58	0.59
EOS	0.92	16.66*	1.94	0.35	8.40*	3.81	1.30	0.01	0.47
DUR	0.06	8.07*	0.34	0.16	8.40*	0.57	0.10	4.80*	0.00
MAXG	11.38*	1.52	5.96*	15.06*	0.20	2.67	7.27*	0.02	0.69

1470 * p-value <0.05

1471

1472

1473

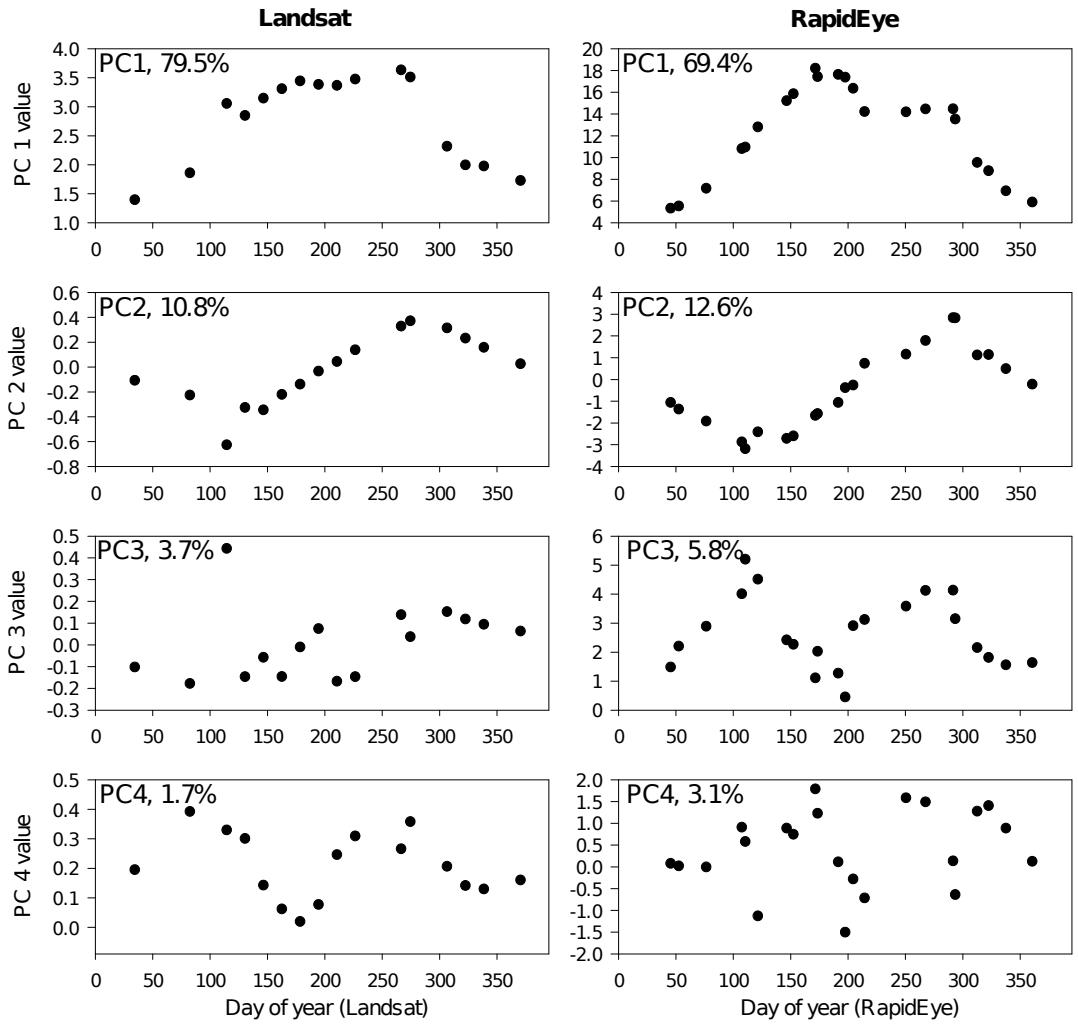
1474 **Supplementary Material**

1475

1476 **A. Selecting pixels for phenological estimation within the**
1477 **biogeochemical footprints**

1478 **Figure S1.** Seasonal trajectories of the first four principal components
1479 (together explaining >90% variation in the data) derived from Landsat (left)
1480 and RapidEye 2016 Enhanced Vegetation Index (EVI) time series of the pixels
1481 inside the biometeorological flux footprints combined among the three
1482 wetland study sites.

1483 Note that PC1 trajectory here is the most consistent with the deciduous
1484 vegetation where the greenness values are expected to be low at the
1485 beginning of the year, then increase until the seasonal maximum is reached
1486 and then decrease again at the end of the growing season. PC2 represents a
1487 similar pattern; however, it is somewhat shifted in time. The early-season
1488 increase in the trajectory is delayed compared to PC1, while the end-of-
1489 season decrease continues into the winter time frame as suggested by the
1490 initial decrease in the trajectory during the days 0-100 as a spillover from the
1491 previous year.



1493 **Table S1.** Selection of pixels for phenological curve fitting based on the
 1494 similarity to deciduous trajectory within the biogeochemical flux footprints of
 1495 three wetland sites represented by the first and second principal
 1496 components (PC1 and PC2, respectively) of the greenness series from each
 1497 satellite product. Here “in mask” denotes pixels included in the subsequent
 1498 phenological analyses.

Metric	Landsat			RapidEye		
	West Pond	Mayberry Farms	East End	West Pond	Mayberry Farms	East End
Total pixel count	33	81	30	928	2234	784
Pixels with ≥ 0.7 correlation to PC1	33	68	21	799	1924	664
Pixels with ≥ 0.7 correlation to PC2	0	0	3	18	0	87
Pixels with ≥ 0.7 correlation to PC1 or PC2 as %total	100%	84%	80%	88%	86%	96%

1499
 1500 **B. Phenological parameter estimation**

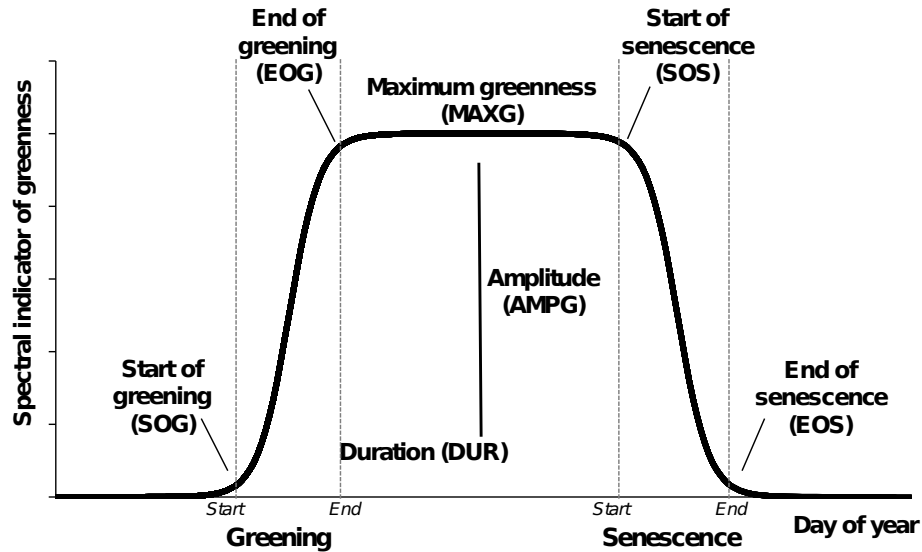
1501
 1502 **1. Double-logistic model for seasonal greenness**

1503 As a proxy of vegetation greenness, we used the Enhanced Vegetation Index
 1504 (EVI) which has been widely used in terrestrial phenological analyses and
 1505 sometimes preferred over other popular indicators due to greater sensitivity
 1506 to vegetation signals in closed canopy setting (Huete et al., 2002; Melaas et
 1507 al., 2016, 2013):

1508
$$EVI = \frac{2.5 * (NIR - i)}{(NIR + 6 * i - 7.5 * i + 1)}, (1)$$

1509 Fitting a curve to per-pixel phenological series of EVI is an important step in
 1510 the analyses because it allows interpolating greenness (spectral vegetation
 1511 index) values from discrete observations of available image dates to a daily
 1512 time step. While a variety of algorithms and functions have been proposed
 1513 for such interpolations, studies focusing on vegetation with deciduous
 1514 seasonality have often considered sigmoid logistic functions consistent with
 1515 the non-linear dynamics of greenness proxies (Figure S2), i.e., more rapid

1516 changes during the early season green-up and late season senescence and
 1517 low variation during the low greenness (i.e., before the start of greening and
 1518 after the end of senescence) and high greenness (between end of greening
 1519 and start of senescence) phases (Gonsamo et al., 2013; Klosterman et al.,
 1520 2014; Misra et al., 2016; Son et al., 2016; Tan et al., 2011; Toomey et al.,
 1521 2015; Xu et al., 2014).



1522 **Figure S2:** Deciduous phenological trajectory represented by a double-
 1523 logistic function.
 1524

1525
 1526 A double-logistic function (Bauer et al., 2017; Head et al., 2004) captures
 1527 both increase (green-up) and decrease (senescence) phases by a single
 1528 equation with different parameter sets for each phase to the Enhanced
 1529 Vegetation Index (EVI) series:

1530

$$EVI(t) = P_1 + \frac{P_2}{1 + e^{P_3(P_{i4} - t)}} + \frac{P_2}{1 + e^{P_5(P_{i6} - t)}} \quad (2)$$

1531 where the parameters P_1, P_2, \dots, P_6 determine the shape and asymmetry in
 1532 the fitted double-logistic curve (Bauer et al., 2017) and t indicates the day of
 1533 year (DOY).

1534
 1535 Fitting the function in (2) as a regression model to the input series of EVI
 1536 involves finding a set of parameter values P_1, P_2, \dots, P_6 which minimize the
 1537 “cost function”, i.e. a measure of error as the distance between the original
 1538 and fitted values. By the nature of model (2), its cost function may have
 1539 more than one local minimum in the multi-dimensional space of its

1540 parameters, which may complicate the search for their best fitting set. To
1541 help achieve the global, rather than local, minimum corresponding to the
1542 least predictive error, it is important to constrain the search space by
1543 providing the initial guess on the parameters P_1, P_2, \dots, P_6 . As such a guess
1544 would be specific to both the shape and the extrema of the individual per-
1545 pixel trajectories, a fixed set of numbers might not be applicable to all the
1546 pixels in the sample, especially in landscapes with high local variation in
1547 greenness. To automate such initial parameter guessing in this study, we
1548 estimated the starting values of P_3, P_4, P_5 and P_6 using the extrema in the first
1549 derivative of a first-order Fourier function fitted to the original pixel EVI
1550 series. The starting values of P_1 and P_2 were approximated by the minimum
1551 and the difference between maximum and minimum, respectively, of the
1552 original EVI series for each pixel.

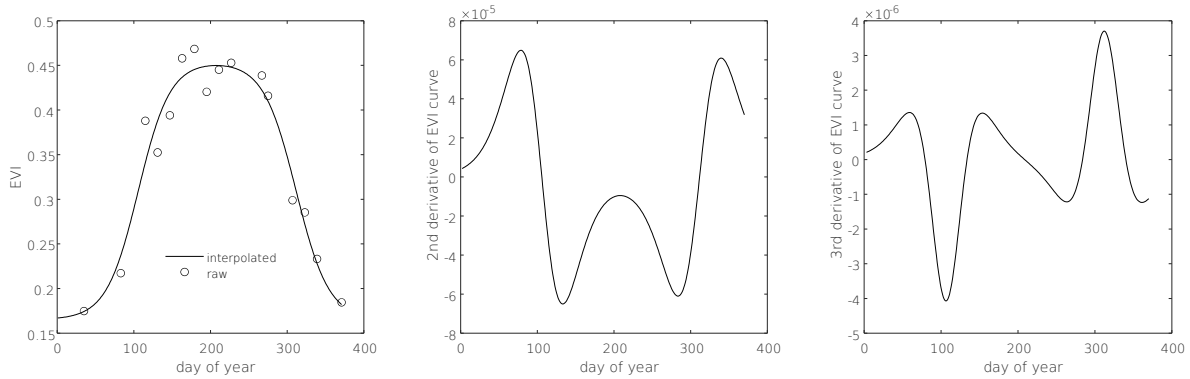
1553

1554

1555 **2. Extracting phenological metrics for the timing of greening and** 1556 **senescence**

1557 Following the fitting of the double-logistic function, curvatures in the pixel
1558 daily interpolated EVI series were used to estimate the start and end dates of
1559 greening and senescence phases and the duration of the growing season
1560 (Figure S2). Such key transitions can be approximated by the local minima
1561 and maxima in the curve derivatives; however, specific choices of the latter
1562 vary among studies. Tan and colleagues (2011) provide a detailed analysis
1563 and interpretation of such curvatures, indicating that the 3rd derivative's
1564 extrema approximate more closely the timing of changes in the actual
1565 curvature of greenness, while the 2nd derivative's extrema represent the
1566 timing when the majority of a pixel changes in greenness. The latter study
1567 preferred 3rd derivative as the primary indicator of the greening and
1568 senescence transitions, more consistent with how they might be detected in
1569 ground-scale phenological observations (Tan et al., 2011). Another study
1570 focusing on a rural landscape with broadleaf forest areas in Germany (Misra
1571 et al., 2016) also recommended the 3rd derivative over 2nd as the former
1572 more effectively captured inter-annual phenological variability and
1573 contributions from the forest understory species. A well-defined double-
1574 logistic curve typically has three prominent peaks and two troughs in the 2nd
1575 derivative and three peaks and three troughs in the 3rd derivative (Figure
1576 S3).

1577



1578
 1579 **Figure S3.** An interpolated double-logistic curve fitted to the raw greenness
 1580 series (left panel) with its second (middle panel) and third (right panel)
 1581 derivatives.

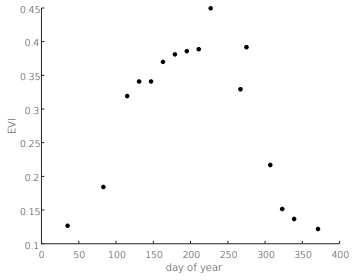
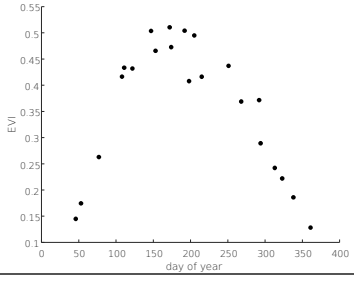
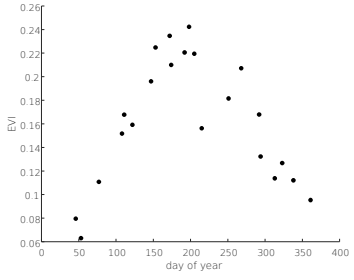
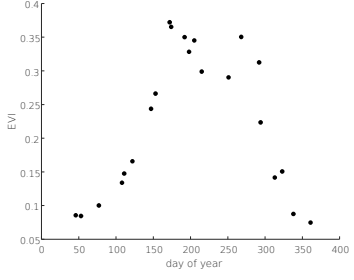
1582

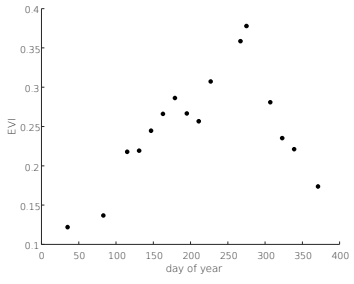
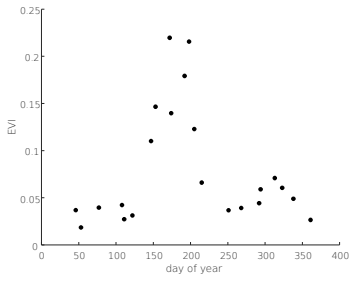
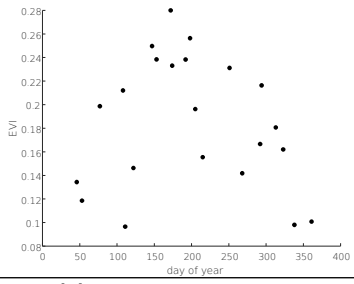
1583 **3. Special cases and challenges in double-logistic fitting**

1584 Many previous phenological studies have focused on “upland” terrestrial
 1585 ecosystems and used moderate to coarse spatial resolution imagery, where
 1586 seasonal change in aboveground vegetation biomass, cover and health are
 1587 often the main contributors to variation in spectral indicators, consistent with
 1588 generalized models such as (2). However, in wetland environments,
 1589 phenological dynamics may show high local heterogeneity due to inundation
 1590 effects on plant reflectance spectra, zoning of plant communities along
 1591 elevation gradients, local disturbance and other factors (Kearney et al.,
 1592 2009; Knox et al., 2017; Mo et al., 2015). For hydrologically managed
 1593 wetlands such as in our study area, we expected that spatial variability in the
 1594 amount and height of litter, dominant species and disturbance such as pest
 1595 outbreaks could be especially important contributors to the local timing of
 1596 green-up and senescence and the specific shape and magnitude of seasonal
 1597 EVI trajectories (Eichelmann et al., 2018; Knox et al., 2017; Rocha et al.,
 1598 2008).

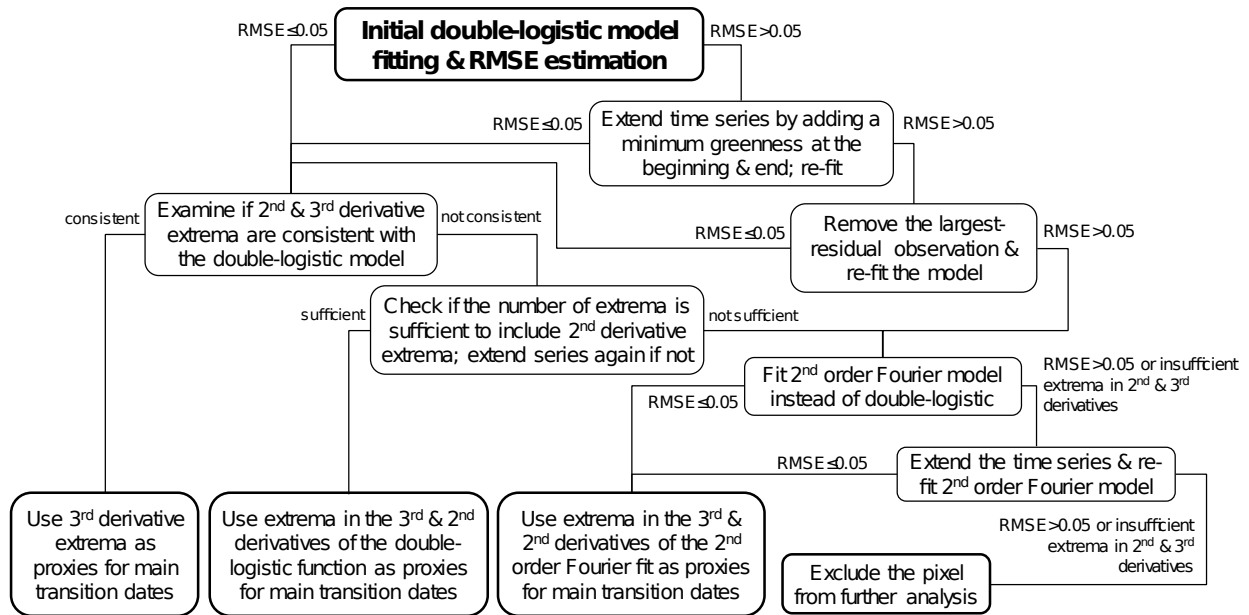
1599 Indeed, initial efforts to fit double-logistic function (2) to per-pixel EVI series
 1600 of our wetland sites revealed that some of the pixel trajectories were difficult
 1601 to accommodate by this model, as summarized in Table S2. Such cases were
 1602 diagnosed using model root mean square error (RMSE) >0.05 and number of
 1603 peaks and troughs in both 2nd and 3rd derivatives inconsistent with the
 1604 double-logistic model (Figure S3), or both (Figure S4). To avoid excluding
 1605 such pixels entirely from the analysis, considering our primary focus on
 1606 analyzing phenological heterogeneity, we adopted a set of corrective
 1607 strategies (Table S2), sometimes applying more than one of them to a given
 1608 pixel (Figure S4).

1609 **Table S2.** Examples of the common challenges in fitting double-logistic
 1610 function to EVI series.

Challenge	Example of EVI series	Potential strategies*
Short-term spike in greenness at the beginning or the end of the peak greenness phase, deviating from the main region of high EVI values but consistent with the overall timing of the higher greenness phase		Remove the observation with the largest residual and re-fit the model.
Insufficient curvature at the very onset of greening and the very end of senescence		To facilitate the fitting, extend the time series by replicating the minimum EVI at 16 days at each end of the series, assuming that the values do not change substantially during the lowest greenness phase.**
Insufficient representation of double-logistic curvature at some stages of greening and/or senescence, leading to fewer than expected extrema in the 3 rd derivative function		Consider 2 nd derivative extrema as the next closest approximation for a given indicator of the greening and/or senescence timing.
Complex variation of EVI values near the peak of the growing season which, however, remains constrained within a certain range of high greenness values		If the 3 rd derivative has 3 maxima and 3 minima, use these extrema as in double-logistic model which may still fit reasonably well to such a series. In case of a more complex trajectory implied by high model RMSE >0.05, use the 2 nd order Fourier fitting function and its derivative extrema.

<p>Complex trajectory with high variation of EVI values at the peak growing season without a well-defined plateau of high greenness values</p>		<p>Use the 2nd order Fourier function and its 2nd and 3rd derivative extrema instead of the double-logistic model; to facilitate the fitting, artificially extend the time series replicating the minimum EVI at 16 days at each end of the series.</p>
<p>Greenness trajectory represents a single peak instead of a plateau</p>		<p>If the 3rd derivative has 3 maxima and 3 minima while the 2nd derivative has 2 maxima and 1 minimum, the case is consistent with the double-logistic model, and the 3rd derivative's extrema can be used for transition dates. If there is insufficient early- or late-season curvature, consider 2rd derivative extrema or, with high model RMSE >0.05, use the 2nd order Fourier function and its derivative extrema.</p>
<p>Substantial noise despite the evidence of the overall seasonal increase and decrease in greenness</p>		<p>If none of the corrective measures achieve a satisfactory level of error, exclude the pixel from the analysis.</p>

- 1611 *Potential strategies presented here are not necessarily mutually exclusive and
1612 more than one strategy may be sometimes used for a particular special case pixel.
1613 **This measure was based on the assumption that late December and January
1614 would be the periods of the lowest greenness for the respective pixels, which would
1615 be also consistent with the general trajectory of phenocam greenness for each
1616 wetland site.



1617
1618
1619
1620

Figure S4. A flowchart diagram representing major steps in curve-fitting.

1621
1622
1623
1624
1625
1626
1627
1628
1629
1630
1631
1632
1633

In some cases, pixel trajectories could not be reasonably approximated by a double-logistic model due to the nature of signal variation. Such were, for instance, cases when the main increase in greenness was accompanied by smaller-magnitude fluctuations during the “low” greenness periods, or when the peak-season greenness values exhibited more complex variation not consistent with either a plateau or a single peak (Table S2). For such pixels, RMSE could remain high or the number of meaningful extrema in 2nd and 3rd derivative could be insufficient even after implementing the initial corrective measures (Figure S4). The second-order Fourier function was considered as an alternative “harmonic regression” model (Brooks et al., 2012; Wallace et al., 2013; Wilson et al., 2018) because it allows representing the expected periodicity of deciduous vegetation greenness while also accommodating some degree of complexity in the main EVI trajectory:

1634

$$EVI(t) = a_0 + \sum_{i=1}^n a_i \cos(iwt) + b_i \sin(iwt) \quad (3)$$

1635
1636
1637
1638
1639
1640
1641

where t is the time (day of year), a_0 is a constant (intercept) related to $i=0$, w is the fundamental frequency of the signal, n is the number of harmonics in the series (here $n=2$ for the second-order function). We then similarly used the extrema of 3rd and, where necessary, 2nd derivatives of the fitted Fourier curve to estimate the days of the key transitions. Overall, such cases were relatively uncommon, representing 0-14% pixels in most sites (Table S3), except for RapidEye pixels at one of our wetlands, the Mayberry Farms site,

1642 where they constituted ~31% of the sample (Table S3) and occurred both
 1643 within water and within vegetated areas.

1644

1645 If for a given pixel none of the corrective measures sufficiently improved the
 1646 fit, that pixel was excluded from the analysis completely. Such excluded
 1647 pixels ultimately constituted for Landsat and RapidEye inputs, respectively,
 1648 3% and 1% of the originally selected pixels at West Pond, 12% & 8% of the
 1649 selected pixels at East End and 4% of pixels with both input products at
 1650 Mayberry Farms (Table S3). Visual examination showed that these cases
 1651 often corresponded to open-water areas where EVI trajectories could be
 1652 influenced by algae, changes in water chemistry and physical disturbance
 1653 affecting spectral values, such as wind-induced ripples. A more detailed list
 1654 of special cases and rules considered in assigning curvatures of the 2nd and
 1655 3rd curve derivatives as key transition dates is provided in Table S4 below.

1656

1657 **Table S3.** Differences in model fitting to pixels from two satellite input
 1658 sources within the wetland site flux footprints.

Metric	Landsat			RapidEye		
	West Pond	Mayberry Farms	East End	West Pond	Mayberry Farms	East End
Pixels with fitted curves (%of in-mask pixels)	32	65	21	807	1850	692
%of in-mask pixels	97%	96%	88%	99%	96%	92%
Pixels with double-logistic fitting	31	65	18	775	1277	612
%all fitted	97%	100%	86%	96%	69%	88%
Pixels with 2 nd order Fourier fitting	1	0	3	31	573	80
%all fitted	3%	0%	14%	4%	31%	12%
Pixels with double-logistic model where transitions were estimated with only 3 rd derivative extrema	30	59	18	598	659	416
%all fitted	97%	91%	100%	77%	52%	68%

1659

1661 **Table S4.** Rules and special cases for approximating phenological transition dates using the timing of the
 1662 curvatures of the 2nd and 3rd derivatives of the fitted functions. Cases where second or third derivatives
 1663 had less than 2 peaks were excluded from estimation. The terms such as “first”, “last”, “penultimate” and
 1664 “earliest” below refer to the timing, i.e., day of year associated with a given curvature.

Number (#) of curvature points (peaks & troughs) in the 2nd & 3rd derivatives of the fitted curve				Phenological transition dates inferred from the timing of the curvatures in the 2nd and/or 3rd derivatives				Special cases, if any
2nd, #peaks	2nd, #troughs	3rd, #peaks	3rd, #troughs	SOG	EOG	SOS	EOS	
<i>Double-logistic curve function</i>								
≥3	2	3	3	First peak of 3 rd	Penultimate peak of 3 rd	Penultimate trough of 3 rd	Last trough of 3 rd	If estimated EOG>SOS, use SOS as last trough of 3 rd and EOS as the last peak of the 2 nd
≥3	2	3	2	First peak of 3 rd	Penultimate peak of 3 rd	Last trough of 3 rd	Last peak of 2 nd	
≥3	3	3	3	First peak of 3 rd	Penultimate peak of 3 rd	Last trough of 3 rd	Last peak of 2 nd	
≥3	3	3	2	First peak of 3 rd	Penultimate peak of 3 rd	Last trough of 3 rd	Last peak of 2 nd	
≥3	2	2	3	First peak of 2 nd	First peak of 3 rd	Penultimate trough of 3 rd	Last trough of 3 rd	
≥3	2	2	2	First peak of 3 rd	Last peak of 3 rd	Last trough of 3 rd	Later of the last peaks of 2 nd & 3 rd	
≥3	3	4	3	First peak of 3 rd	Second peak of 3 rd	Penultimate trough of 3 rd	Last trough of 3 rd	
≥3	3	3	4	First peak of 3 rd	Penultimate peak of 3 rd	Penultimate trough of 3 rd	Last trough of 3 rd	
≥3	2	4	3	First peak of 3 rd	Second peak of 3 rd	Penultimate trough of 3 rd	Later of the last troughs of 2 nd & 3 rd	
3	1	2	3	First trough of 3 rd	First peak of 3 rd	Penultimate trough of 3 rd	Last trough of 3 rd	

						3 rd		
3	1	3	2	First peak of 3 rd	Penultimate peak of 3 rd	Penultimate peak of 2 nd	Last peak of 2 nd	
2	2	3	3	First peak of 3 rd	Penultimate peak of 3 rd	Penultimate trough of 3 rd	Last trough of 3 rd	If penultimate peak of 3 rd is later than penultimate trough of 3 rd , use SOS as penultimate peak of 3 rd and EOS as the last peak of 2 nd
2	2	3	2	First peak of 3 rd	Penultimate peak of 3 rd	Last trough of 3 rd	Last peak of 3 rd	If estimated EOG>SOS, approximate both EOG & SOS as the first trough of 3 rd
2	2	2	3	Earlier of the first peak of 3 rd & the first trough of 2 nd	Last trough of 2 nd	Last peak of 3 rd	Last trough of 3 rd	
2	3	3	3	First peak of 2 nd	Penultimate trough of 2 nd	Last trough of 3 rd	Last peak of 3 rd	
2	3	2	2	First peak of 2 nd	Penultimate trough of 2 nd	Penultimate trough of 2 nd	Last trough of 3 rd	
2	3	3	2	First peak of 2 nd	Penultimate trough of 2 nd	Penultimate trough of 2 nd	Last trough of 3 rd	
2	3	2	3	First peak of 3 rd	Penultimate trough of 2 nd	Penultimate trough of 3 rd	Last trough of 3 rd	
2	1	3	3	First peak of 3 rd	Penultimate peak of 3 rd	Penultimate trough of 3 rd	Last trough of 3 rd	
2	1	3	2	First peak of 3 rd	Penultimate peak of 3 rd	Later of the penultimate peak of 3 rd & last trough of 3 rd	Last peak of 2 nd	

2	2	3	4	First peak of 3 rd	Penultimate peak of 3 rd	Penultimate trough of 3 rd	Last trough of 3 rd	
4	3	3	3	First peak of 3 rd	Penultimate trough of 2 nd	Penultimate trough of 3 rd	Last trough of 3 rd	
<i>Fourier function:</i>								
3	2	3	3	First peak of 3 rd	Penultimate peak of 3 rd	Penultimate trough of 3 rd	Last trough of 3 rd	If estimated EOG>SOS, use the last peak of 2 nd for SOS
3	2	3	2	First peak of 2 nd	First trough of 2 nd	Penultimate peak of 3 rd	Later of the last peaks of 2 nd & 3 rd	
3	2	2	2	Earliest of the first peak of 2 nd & first trough of 3 rd	First peak of 3 rd	Same as EOG (single-peak trajectory)	Later of the last peaks of 2 nd & 3 rd	Special case if predicted EVI at the first peak of 3 rd is greater than EVI at the last troughs of both 2 nd & 3 rd derivatives. Additionally, for EOG & SOS use last trough of 3 rd if the absolute difference in EVI between first peak of 3 rd & last trough of 3 rd is <0.1, and use the last trough of 2 nd if the absolute difference in EVI between the first peak of 3 rd & last trough of 2 nd <0.1
				Earliest of the first peak of 2 nd & first trough of 3 rd	First trough of 3 rd	Same as EOG (single-peak trajectory)	Later of the last peaks of 2 nd & 3 rd	Special case if predicted EVI at the last trough of 3 rd >EVI at the last trough of 2 nd
				Earliest of the first peak of 2 nd	First trough of 2 nd	Same as EOG (single-peak trajectory)	Later of the last peaks of 2 nd & 3 rd	Special case if predicted EVI at the last trough of 3 rd <EVI at the last

				& first trough of 3 rd		peak trajectory)		trough of 2 nd
3	2	2	3	First peak of 2 nd	First peak of 3 rd	Penultimat e trough of 3 rd	Last peak of 2 nd	
3	3	3	2	First peak of 3 rd	Penultimate peak of 3 rd	Penultimat e peak of 3 rd	Last peak of 3 rd	
3	3	4	3	First peak of 3 rd	Second peak of 3 rd	Penultimat e trough of 3 rd	Last trough of 3 rd	
3	3	3	3	Earlier of the first peaks of 2 nd & 3 rd	Penultimate trough of 2 nd	Penultimat e peak of 3 rd	Last peak of 3 rd	
2	2	2	3	Earlier of the first peak of 3 rd & first trough of 2 nd	Last trough of 2 nd	Last trough of 2 nd	Last trough of 3 rd	
2	2	3	3	First peak of 3 rd	Second peak of 3 rd	Second peak of 3 rd	Last peak of 2 nd	
2	2	3	2	First peak of 2 nd	First trough of 2 nd	Penultimat e peak of 3 rd	Last peak of 3 rd	
2	3	2	3	First peak of 2 nd	Second trough of 2 nd	Second trough of 2 nd	Last peak of 2 nd	
2	3	3	3	First peak of 3 rd	Second trough of 2 nd	Second trough of 2 nd	Later of the last peak of 3 rd & the last trough of 2 nd	
2	3	3	2	First peak of 2 nd	Second trough of 2 nd	Second trough of 2 nd	Last trough of 3 rd	
2	3	2	2	First peak of 2 nd	First peak of 3 rd	Same as EOG	Later of the last peaks of 2 nd & 3 rd	Special case if predicted EVI at the first peak of 3 rd is greater than EVI at the last troughs of both

2 nd & 3 rd derivatives								
2	3	2	2	First peak of 2 nd	First trough of 3 rd	Same as EOG	Later of the last peaks of 2 nd & 3 rd	Special case if predicted EVI at the last trough of 3 rd > EVI at the last trough of 2 nd
2	3	2	2	First peak of 2 nd	First trough of 2 nd	Same as EOG	Later of the last peaks of 2 nd & 3 rd	Special case if predicted EVI at the last trough of 3 rd < EVI at the last trough of 2 nd
2	1	3	2	First peak of 2 nd	Second peak of 3 rd	Second peak of 3 rd	Last peak of 3 rd	
<i>Additional cases considered if model RMSE < 0.05</i>								
2	2	2	1	Earlier of the first peak of 3 rd & first trough of 2 nd	Trough of the 3 rd (one value)	Last trough of the 2 nd	Last peak of the 2 nd	
2	2	2	2	Earlier of the first peak of 2 nd & first trough of 3 rd	Earlier of the two values with the highest predicted EVI within the set including first peak of 3 rd , first trough of 2 nd , last trough of 3 rd & last trough of 2 nd	Later of the two latest values with the highest predicted EVI within the set including first peak of 3 rd , first trough of 2 nd , last trough of 3 rd & last trough of 2 nd	Last peak of the 3 rd	Estimation of EOG and SOS requires a special adjustment because their correspondence to peaks vs troughs depended on the (as)symmetry of the overall fitted curve which could vary depending on a pixel's time series

1665

1666

1667 **4. References for Supplementary Material**

- 1668 Bauer, L.G.M., Hametner, B., Mayer, C.C., Wassertheurer, S., 2017.
1669 Mathematical Wave Fitting Models for the Quantification of the Diurnal
1670 Profile and Variability of Pulse Wave Analysis Parameters. *SNE*
1671 *Simulation Notes Europe* 27, 153-160.
1672 <https://doi.org/10.11128/sne.27.tn.10386>
- 1673 Brooks, E.B., Thomas, V.A., Wynne, R.H., Coulston, J.W., 2012. Fitting the
1674 Multitemporal Curve: A Fourier Series Approach to the Missing Data
1675 Problem in Remote Sensing Analysis. *IEEE Transactions on Geoscience*
1676 *and Remote Sensing* 50, 3340-3353.
1677 <https://doi.org/10.1109/TGRS.2012.2183137>
- 1678 Eichelmann, E., Hemes, K.S., Knox, S.H., Oikawa, P.Y., Chamberlain, S.D.,
1679 Sturtevant, C., Verfaillie, J., Baldocchi, D.D., 2018. The effect of land
1680 cover type and structure on evapotranspiration from agricultural and
1681 wetland sites in the Sacramento-San Joaquin River Delta, California.
1682 *Agricultural and Forest Meteorology* 256-257, 179-195. [https://doi.org/](https://doi.org/10.1016/j.agrformet.2018.03.007)
1683 [10.1016/j.agrformet.2018.03.007](https://doi.org/10.1016/j.agrformet.2018.03.007)
- 1684 Gonsamo, A., Chen, J.M., D'Odorico, P., 2013. Deriving land surface
1685 phenology indicators from CO2 eddy covariance measurements.
1686 *Ecological Indicators* 29, 203-207.
1687 <https://doi.org/10.1016/j.ecolind.2012.12.026>
- 1688 Head, G.A., Lukoshkova, E.V., Mayorov, D.N., van den Buuse, M., 2004. Non-
1689 symmetrical double-logistic analysis of 24-h blood pressure recordings
1690 in normotensive and hypertensive rats: *Journal of Hypertension* 22,
1691 2075-2085. <https://doi.org/10.1097/00004872-200411000-00008>
- 1692 Huete, A., Didan, K., Miura, T., Rodriguez, E.P., Gao, X., Ferreira, L.G., 2002.
1693 Overview of the radiometric and biophysical performance of the MODIS
1694 vegetation indices. *Remote Sensing of Environment* 83, 195-213.
1695 [https://doi.org/10.1016/S0034-4257\(02\)00096-2](https://doi.org/10.1016/S0034-4257(02)00096-2)
- 1696 Kearney, M.S., Stutzer, D., Turpie, K., Stevenson, J.C., 2009. The Effects of
1697 Tidal Inundation on the Reflectance Characteristics of Coastal Marsh
1698 Vegetation. *Journal of Coastal Research* 25, 1177-1186. [https://doi.org/](https://doi.org/10.2112/08-1080.1)
1699 [10.2112/08-1080.1](https://doi.org/10.2112/08-1080.1)
- 1700 Klosterman, S.T., Hufkens, K., Gray, J.M., Melaas, E., Sonnentag, O., Lavine,
1701 I., Mitchell, L., Norman, R., Friedl, M.A., Richardson, A.D., 2014.
1702 Evaluating remote sensing of deciduous forest phenology at multiple
1703 spatial scales using PhenoCam imagery. *Biogeosciences* 11, 4305-
1704 4320. <https://doi.org/10.5194/bg-11-4305-2014>
- 1705 Knox, S.H., Dronova, I., Sturtevant, C., Oikawa, P.Y., Matthes, J.H., Verfaillie,
1706 J., Baldocchi, D., 2017. Using digital camera and Landsat imagery with
1707 eddy covariance data to model gross primary production in restored
1708 wetlands. *Agricultural and Forest Meteorology* 237, 233-245.
1709 <https://doi.org/10.1016/j.agrformet.2017.02.020>
- 1710 Melaas, E.K., Friedl, M.A., Zhu, Z., 2013. Detecting interannual variation in
1711 deciduous broadleaf forest phenology using Landsat TM/ETM plus data.

1712 Remote Sensing of Environment 132, 176–185. <https://doi.org/10.1016/>
1713 [j.rse.2013.01.011](https://doi.org/10.1016/j.rse.2013.01.011)

1714 Melaas, E.K., Sulla-Menashe, D., Gray, J.M., Black, T.A., Morin, T.H.,
1715 Richardson, A.D., Friedl, M.A., 2016. Multisite analysis of land surface
1716 phenology in North American temperate and boreal deciduous forests
1717 from Landsat. *Remote Sensing of Environment* 186, 452–464.
1718 <https://doi.org/10.1016/j.rse.2016.09.014>

1719 Misra, G., Buras, A., Menzel, A., 2016. Effects of Different Methods on the
1720 Comparison between Land Surface and Ground Phenology—A
1721 Methodological Case Study from South-Western Germany. *Remote*
1722 *Sensing* 8, 753. <https://doi.org/10.3390/rs8090753>

1723 Mo, Y., Momen, B., Kearney, M.S., 2015. Quantifying moderate resolution
1724 remote sensing phenology of Louisiana coastal marshes. *Ecological*
1725 *Modelling* 312, 191–199.
1726 <https://doi.org/10.1016/j.ecolmodel.2015.05.022>

1727 Rocha, A.V., Potts, D.L., Goulden, M.L., 2008. Standing litter as a driver of
1728 interannual CO₂ exchange variability in a freshwater marsh. *Journal*
1729 *of Geophysical Research-Biogeosciences* 113, G04020.
1730 <https://doi.org/10.1029/2008JG000713>

1731 Son, N.-T., Chen, C.-F., Chang, L.-Y., Chen, C.-R., Sobue, S.-I., Minh, V.-Q.,
1732 Chiang, S.-H., Nguyen, L.-D., Lin, Y.-W., 2016. A logistic-based method
1733 for rice monitoring from multitemporal MODIS-Landsat fusion data.
1734 *European Journal of Remote Sensing* 49, 39–56.
1735 <https://doi.org/10.5721/EuJRS20164903>

1736 Tan, B., Morissette, J.T., Wolfe, R.E., Gao, F., Ederer, G.A., Nightingale, J.,
1737 Pedelty, J.A., 2011. An Enhanced TIMESAT Algorithm for Estimating
1738 Vegetation Phenology Metrics From MODIS Data. *IEEE J. Sel. Top. Appl.*
1739 *Earth Observations Remote Sensing* 4, 361–371.
1740 <https://doi.org/10.1109/JSTARS.2010.2075916>

1741 Toomey, M., Friedl, M.A., Frohling, S., Hufkens, K., Klosterman, S., Sonnentag,
1742 O., Baldocchi, D.D., Bernacchi, C.J., Biraud, S.C., Bohrer, G., Brzostek,
1743 E., Burns, S.P., Coursolle, C., Hollinger, D.Y., Margolis, H.A.,
1744 McCaughey, H., Monson, R.K., Munger, J.W., Pallardy, S., Phillips, R.P.,
1745 Torn, M.S., Wharton, S., Zeri, M., Richardson, A.D., 2015. Greenness
1746 indices from digital cameras predict the timing and seasonal dynamics
1747 of canopy-scale photosynthesis. *Ecological Applications* 25, 99–115.
1748 <https://doi.org/10.1890/14-0005.1>

1749 Wallace, C.S.A., Villarreal, M.L., van Riper III, C., 2013. Influence of monsoon-
1750 related riparian phenology on yellow-billed cuckoo habitat selection in
1751 Arizona. *Journal of Biogeography* 40, 2094–2107.
1752 <https://doi.org/10.1111/jbi.12167>

1753 Wilson, B.T., Knight, J.F., McRoberts, R.E., 2018. Harmonic regression of
1754 Landsat time series for modeling attributes from national forest
1755 inventory data. *ISPRS Journal of Photogrammetry and Remote Sensing*
1756 137, 29–46. <https://doi.org/10.1016/j.isprsjprs.2018.01.006>

1757 Xu, H., Twine, T., Yang, X., 2014. Evaluating Remotely Sensed Phenological
1758 Metrics in a Dynamic Ecosystem Model. Remote Sensing 6, 4660-4686.
1759 <https://doi.org/10.3390/rs6064660>
1760
1761